Non-peer-reviewed EarthArXiv preprint; submitted to Remote Sensing of Environment (Elsevier).

Land subsidence in Jakarta in Three Dimensions (2014–2025) using InSAR–GNSS Datum Connection and the Strapdown Decomposition

Alexandru M. Lapadat[a,*], Heri Andreas[b], Wietske S. Brouwer[a], Simon A.N. van Diepen[a], Dhota Pradipta[b], Ramon F. Hanssen[a]

[a] *Mathematical Geodesy and Positioning, Delft University of Technology, Stevinweg 1, Delft, Netherlands*
[b] *Geodesy Research Division, Institute of Technology Bandung, Jl. Ganesha 10, Bandung, Indonesia*

Abstract

Coastal megacities face compounding hazards from rising sea levels and land subsidence. Jakarta, one of the fastest-sinking megacities, already experiences recurrent flooding amplified by rapid land subsidence. Assessing and mitigating this hazard requires reliable estimates of three-dimensional ground motion over wide spatial and temporal scales in a well-defined geodetic reference frame and datum. Here we combine spaceborne InSAR and GNSS measurements. We develop a datum connection procedure that aligns multi-track InSAR line-of-sight datasets between 2014 and 2025 to a common datum for unbiased three-dimensional velocity decomposition, and connect the resulting displacement field to the Sunda plate-fixed frame using GNSS, yielding a 3D characterization of Jakarta's land deformation in a globally consistent reference frame. Our results show that Jakarta's land motion is dominated by six main subsidence bowls, with subsidence and directional horizontal rates of up to −7.9 cm/yr and 1.7 cm/yr, respectively, overlying slow regional subsidence of −0.9 cm/yr across the metropolitan area. As these results hinge

*Corresponding author
Email address: A.M.Lapadat@tudelft.nl (Alexandru M. Lapadat)

on the availability of one single continuous GNSS station, we recommend the installation of dedicated geodetic ground-based infrastructure to ensure sustainable and rigorous monitoring capabilities for the future.

Keywords: InSAR, GNSS, datum, geodesy, land subsidence, Jakarta

1. Introduction

Jakarta, the world's most populous city with close to 42 million residents (United Nations, 2025), is among the fastest-sinking megacities on Earth. Historically, using observations since 1925 (Schepers, 1926; Schuitenvoerder, 1926), subsidence occurred at two distinct scales: a citywide north-dipping tilt spanning ∼30 km[1], with rates declining from −4.5 cm/yr in the north to near-zero in the south, and localized subsidence bowls superimposed on this trend, whose extent and intensity vary spatiotemporally, with maximum rates ranging from −7 to −15 cm/yr (Abidin et al., 2001, 2011, 2022). Currently, ∼15% of Jakarta's land area—mainly in the northern districts—already lies below mean sea level, leaving these areas prone to inundation during ordinary high tides (Juliandri et al., 2022). While citywide catastrophic floods in the past decade have been mostly driven by extreme rainfall and river runoff, in North Jakarta it is the subsidence that is causing recurrent tidal flooding, a risk further intensified by ongoing regional sea-level rise (Fenoglio-Marc et al., 2012). Jakarta's subsidence is attributed to three interacting mechanisms: (i) natural compaction of young Quaternary coastal alluvium, (ii) increased effective stress from the load of dense urban development and infrastructure, and (iii) groundwater extraction, which reduces pore pressure in the aquifer system and induces localized, bowl-shaped subsidence (Murdohardono and Sudarsono, 1998; Abidin et al., 2001; Colbran, 2009; Batubara et al., 2023). While natural compaction and loading act gradually, groundwater withdrawal produces rapid and spatially concentrated deformation. The combined effects are structural damage to buildings, cracking and tilting (Abidin et al., 2015; Nugraha et al., 2024), and recurrent flooding (Takagi et al., 2016; Sagala et al., 2013; Firman et al., 2011; Lubis et al., 2022), making land subsidence one of the most critical hazards for Jakarta's long-term sustainability. The combined processes (Abidin et al., 2022; Bennett et al., 2023; Lubis et al., 2022; Colbran, 2009; Takagi et al., 2016; Sagala et al., 2013; Firman et al.,

[1]from Ancol to Pasar Rebo

2011) of land subsidence, sea-level rise, extreme precipitation, and runoff put Jakarta at risk, with subsidence amplifying hazards by lowering ground elevation, increasing coastal flood exposure, and accelerating runoff. These impacts make precise estimation and continuous monitoring of land subsidence essential for effective risk assessment and flood mitigation (Abidin et al., 2015).

Over the past four decades, a range of geodetic techniques (Abidin et al., 2004) have been applied, each with distinct strengths and limitations. Spirit leveling in the 1980s (Abidin et al., 2001; Ekkelenkamp, 2019; Schepers, 1926; Schuitenvoerder, 1926) provided millimeter-level precision but was costly, slow, and spatially sparse. Of the 45 benchmarks established in 1982 (Abidin et al., 2001), many have since disappeared due to Jakarta's rapid urban development. GNSS campaigns from the 1990s onward (Abidin et al., 2001, 2008; Abdullah et al., 2021; Susilo et al., 2023) expanded from 13 benchmarks to 65 by 2010, improving spatial coverage and revealing broader subsidence patterns, but in the meantime several benchmarks became unobservable due to monument destruction (Abidin et al., 2011). Thus, for both leveling and GNSS, the loss or inaccessibility of benchmarks limits the temporal continuity and spatial completeness of the subsidence record. The introduction of spaceborne Interferometric Synthetic Aperture Radar (InSAR) (Hanssen, 2001) in the 1990s revolutionized monitoring, offering dense spatial coverage and frequent temporal sampling across Jakarta's metropolitan area (Abidin et al., 2005, 2011). Early InSAR studies (Abidin et al., 2005; Ng et al., 2012; Koudogbo et al., 2012; Chaussard et al., 2013; Widodo et al., 2019) from Jakarta relied on short, single-track SAR datasets and suffered from temporal decorrelation (Zebker and Villasenor, 1992). Advances in processing methods (e.g., Persistent Scatterer Interferometry (PSI) (Ferretti et al., 2002b,a) and Small Baseline Subset (SBAS) (Berardino et al., 2003; Hooper, 2008)) combined with greater computational capacity, have enabled longer time series and multi-track coverage (Hakim et al., 2020; Zhang et al., 2025; Sidiq et al., 2025).

As InSAR observes the projection of the 3D displacement vector onto the radar line of sight (LoS), these estimates are often projected onto the vertical (PoV), an error-free operation only if horizontal displacements are negligible (Brouwer and Hanssen, 2023). Consequently, vertical PoV displacements are biased in localized subsidence bowls. Although Harintaka et al. (2024) combined ascending and descending tracks to estimate the projection of the displacement onto the east–up plane, the result remains biased due to omission of the north component (Brouwer and Hanssen, 2023). Therefore, no InSAR product currently provides a complete three-dimensional and unbiased view of ground motion in Jakarta.

Nearly all InSAR-based velocity maps of Jakarta are relative, given in an arbitrary local InSAR datum. The physical 'null-location', where the displacement rate is 0 mm/yr, is unknown. This rank defect can result in misleading geophysical interpretations, such as apparent uplift in central Jakarta (Widodo et al., 2019; Zhang et al., 2025), which is physically unrealistic. Consequently, studies focusing on fast-subsiding bowls driven by groundwater extraction may overlook slower, widespread regional subsidence, which can be obscured if the InSAR datum is not linked to a plate-fixed reference frame, such as the Sunda plate-fixed frame (Yong et al., 2017). In fact, only a few studies have rigorously explored GNSS-based datum connections that link InSAR to a terrestrial reference frame (Mahapatra et al., 2018; Su et al., 2026), underscoring the need for a robust 3D datum connection procedure.

Using a modified strapdown decomposition (Brouwer and Hanssen, 2024) that jointly estimates 3D velocities and aligns multi-track InSAR data to a common datum, followed by a final GNSS-based connection to a terrestrial reference frame, we present the first estimation of three-dimensional velocity vectors across Jakarta in the Sunda plate-fixed frame. In Sec. 2 we present the input datasets and the methodology for multi-track InSAR alignment and GNSS-based datum connection of the InSAR velocity map to the Sunda plate-fixed frame. In Sec. 3, we apply the method to two InSAR track velocity datasets to obtain 3D velocities aligned to a common InSAR datum. We then estimate the velocity offset between this local InSAR datum and the Sunda plate-fixed frame at the location of a continuously operating GNSS reference station (CORS) and apply it uniformly to all provisory 3D velocities, producing the final 3D velocity field for Jakarta in the Sunda plate-fixed frame. This final 3D velocity field is validated using an independent co-located GNSS site. Sec. 4 presents the resulting subsidence patterns, and the final section summarizes the key findings and their implications for Jakarta.

2. Methodology

We subsequently discuss the input datasets and the decomposition assumptions, followed by the inter-track datum alignment establishing a common

InSAR datum, and a procedure for estimating the motion of this common InSAR datum within the Sunda plate-fixed frame.

2.1. Dataset Preparation

We use two datasets of InSAR Point Scatterer[2] (PS) LoS displacement time series spanning 2014–2025, see Fig. 1. The datasets were generated from 281

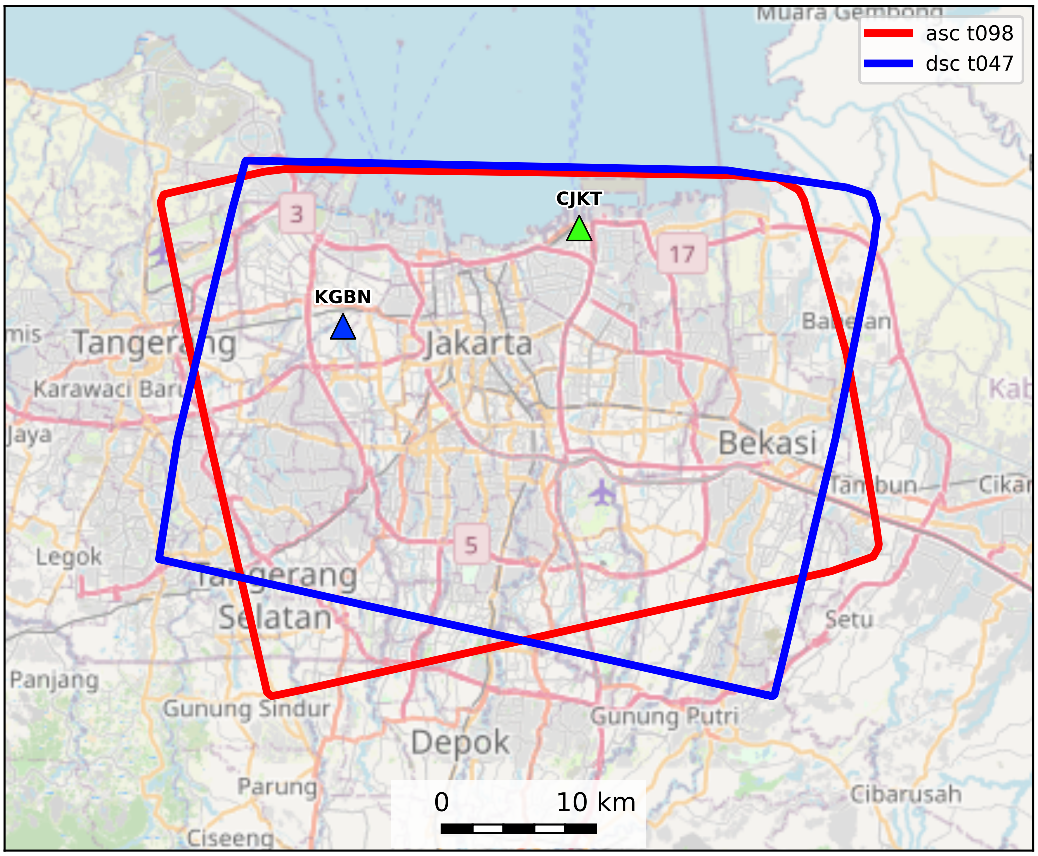

Figure 1: Area of Interest (AOI) covering the Jakarta metropolitan area, showing the Sentinel-1 ascending (track 98, red) and descending (track 47, blue) footprints. The location of the CORS GNSS station CJKT used for datum alignment is indicated as a green triangle, and the GNSS station KBGN, used to validate the final 3D velocity field, is indicated by a blue triangle

.

[2]We use the Delft taxonomy for scatterer classification, see (Hu et al., 2019).

Sentinel-1 acquisitions from ascending track 98 and 183 acquisitions from descending track 47, using the Delft implementation of Persistent Scatterer Interferometry, DePSI (Kampes, 2006; Van Leijen, 2014). We adopt a linear velocity parametrization for all subsequent estimates, supported by post-fit residual analysis and hypothesis testing, see Sup. B. Each track uses a unique local datum defined by its mean linear velocity. Consequently, all velocities are relative and must be interpreted in terms of the spatial variability.

Additionally, we use GNSS observations from two stations with distinct roles, see Fig. 1. Station CJKT is used to align the common InSAR datum with the Sunda plate-fixed frame, whereas station KBGN provides a representative site for independent validation of the final 3D velocity field. CJKT is a CORS located at Tanjung Priok and operated by Badan Informasi Geospasial (BIG). Its antenna is mounted on a 2 m tall concrete pillar on the roof of a two-story concrete building, see Fig. 2D. This station is the only existing long-term CORS in Jakarta that was operational during the 2014–2025 InSAR observation period. Its daily station coordinates were derived from continuous GPS phase observations collected between October 2010 and January 2022.[3]

Station KBGN is located in Kembangan, north-west Jakarta, and was installed by the Jakarta Survey Division for continuous land-subsidence monitoring. The station is monumented on a metal pole founded to 1 m depth. Its daily station coordinates were estimated from available GPS code and phase observations within 2023–2025.[4]

To express the GNSS time series in the Sunda plate-fixed frame, we re-

[3]The CJKT GNSS data were processed by Susilo et al. (2023) in differential mode using the GAMIT/GLOBK software package version 10.71 (Herring et al., 2010). Daily station positions were estimated using double-differenced, ionosphere-free phase observations with respect to 12 IGS reference stations, applying precise IGS orbits, atmospheric delay modelling, and standard tidal and loading corrections. The daily solutions were subsequently combined and aligned in GLOBK to IGb14—the International GNSS Service (IGS) reference frame aligned with ITRF2014—using eight stable global reference stations.

[4]The KBGN GNSS data were processed via ambiguity-resolved precise point positioning in PRIDE-PPP A.R software package version 3.2.8 (Geng et al., 2019). The processing used Wuhan University WUM rapid products, including satellite orbits, clocks, code/phase biases, Earth-rotation parameters, and satellite attitude information. Antenna phase-centre corrections were applied using the IGS ANTEX model in the IGS20/ITRF2020 reference frame, yielding daily station coordinates in ITRF2020.

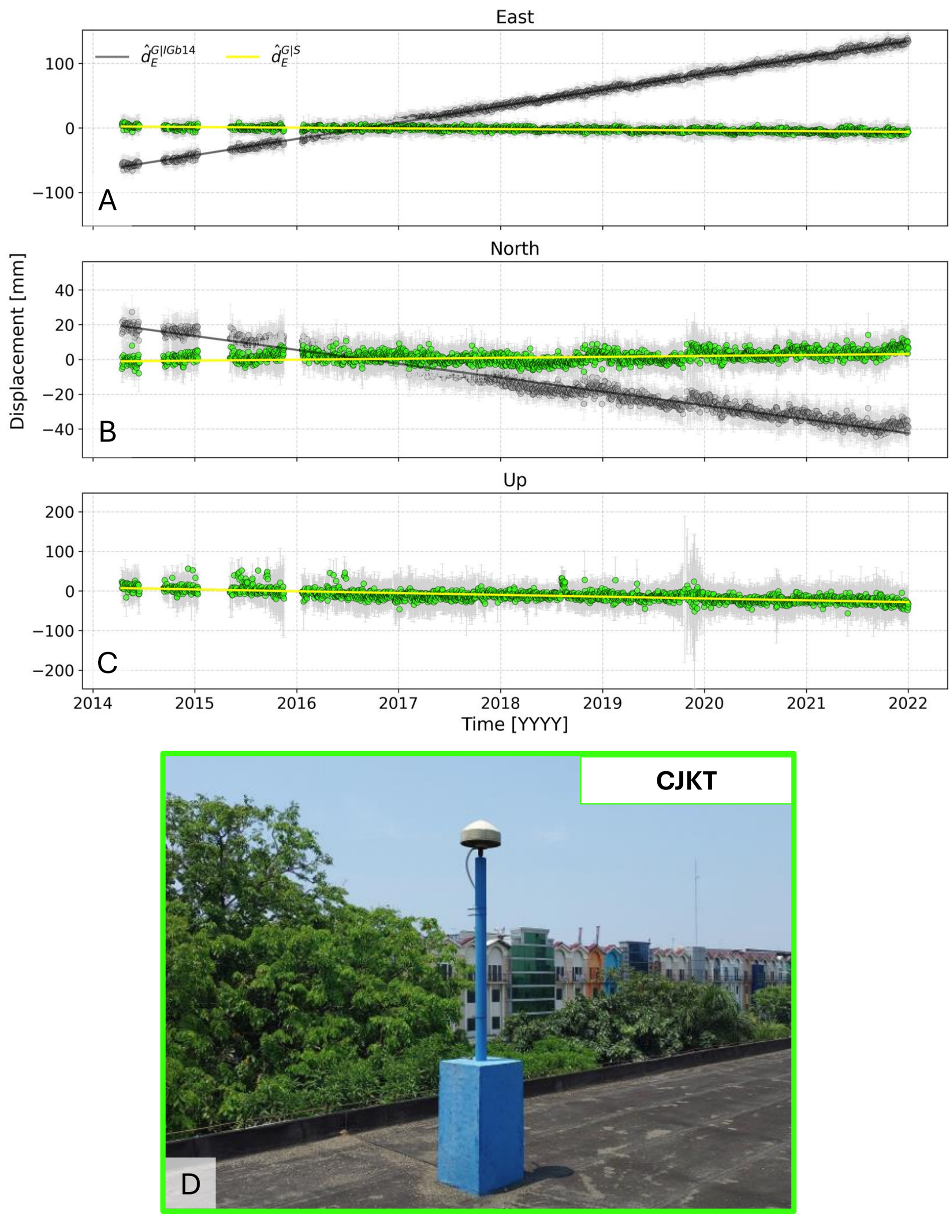

Figure 2: (A–C) East, North, and Up displacement time series of the CJKT GNSS station (2014–2022) with 2σ uncertainties. Grey markers show IGb14 displacements, while green markers show the time series expressed in the Sunda plate-fixed frame after removing Sunda Plate motion using the GSRM v2.1 model. This removal eliminates the southeast horizontal plate motion of 26.52 ± 0.05 mm/yr, yielding near-zero horizontal velocity. The corresponding 3D linear velocities in both reference frames are reported in Tab. 1. (D) CJKT GNSS configuration, located on the roof of a two-story concrete building, supported on deep piles.

Table 1: Linear velocities of GNSS station CJKT in the IGb14 ($\hat{d}^{G|\mathrm{IGb14}}$) and Sunda Plate-fixed ($\hat{d}^{G|\mathrm{S}}$) reference frames, corresponding to the linear models fitted to the displacement time series in Fig. 2, with 2σ uncertainties. The Sunda plate-fixed frame values show small residual horizontal motion after plate-motion removal, likely reflecting limitations of the plate-motion model or local monument motion.

	$\hat{d}^{G\|\mathrm{IGb14}}$ [mm/yr]	$\hat{d}^{G\|\mathrm{S}}$ [mm/yr]
East	25.28 ± 0.05	-1.06 ± 0.05
North	7.99 ± 0.04	0.54 ± 0.04
Up	-4.6 ± 0.2	-4.6 ± 0.2

moved the rigid motion of the Sunda Plate using the GSRM v2.1 plate-motion model (Kreemer et al., 2014)[5]. The GNSS timeseries of CJKT and KBGN—originally expressed in IGb14 and ITRF2020, respectively—were first transformed to IGS08/ITRF2008. For each station, the horizontal Sunda Plate velocity was then computed from the plate-motion model, propagated linearly over the corresponding observation period, and subtracted from the time series. This yields GNSS displacement time series in the Sunda plate-fixed frame, as shown for CJKT in Figs. 2A–C.

To ensure consistency with the InSAR velocity estimates, the CJKT 3D displacement time series and associated 2σ-uncertainties were restricted to the overlapping 2014–2022 InSAR period and fitted with a linear-rate model in the Sunda plate-fixed frame. The resulting CJKT velocities before and after removal of Sunda Plate motion are summarized in Tab. 1. For station KBGN, a linear 3D velocity was estimated over its available observation period and used solely for validation, see Sec. 3.2.

2.2. LoS decomposition to 3D velocity

To convert the InSAR LoS velocities[6] into physically meaningful 3D components, we apply the strapdown decomposition method (Brouwer and Hanssen, 2024, 2021), which transforms ascending and descending LoS observations into a local transversal-longitudinal-normal (TLN) coordinate system (Chang et al., 2018), and subsequently to an east-north-up (ENU) coordinate system (Brouwer and Hanssen, 2024).

[5]Euler pole and angular velocity in the IGS08/ITRF2008 realization.

[6]see Sup. `los_velocity_input.png`

First, the method assumes that deformation within each region of uniform motion (RUM), defined here as a 450×450 m area, is spatially constant, i.e., all PS within the RUM share the same displacement behavior and average linear velocity. In this study, the RUM size of 450×450 m is chosen to preserve deformation homogeneity while retaining sufficient PS sampling for reliable spatial statistics, with at least 50 PS per track per RUM. For the strapdown decomposition, the input observations consist of track-specific RUM-averaged velocities, see Sup. A, computed as the robust median[7] of all PS LoS velocities within each RUM. This yields two representative velocities per RUM, one per viewing geometry, which serve as the observations for the decomposition. In principle, the velocity variability and contributing PS within each RUM should be evaluated individually, discarding anomalous PS where justified, as done for the RUM used to connect to the Sunda plate-fixed frame. Second, as the local TLN frame is right-handed, with the longitudinal direction tangential to the iso-displacement contours and the transversal direction defined positive downslope, i.e., toward increasing subsidence, centripetal motion in a subsidence bowl is represented by positive transversal velocity estimates.

The initial TLN coordinate system orientation (Brouwer and Hanssen, 2024) is approximated using three angles: Λ, the azimuth of the longitudinal direction relative to geographic north, initialized by computing the 2D gradient of LoS velocities projected onto the vertical; Φ, the elevation angle of the longitudinal direction relative to the horizontal; and Ω, the elevation angle of the transversal direction. Based on Jakarta's relatively flat terrain, with topographic slopes less than 2° (Abidin et al., 2005), we assume and set $\Phi = \Omega = 0$. Conservative uncertainties of $\sigma_\Lambda = 10°$, and $\sigma_\Phi = \sigma_\Omega = 3°$ are assigned to account for potential imperfections in the TLN orientation, yielding quality metrics for the ENU displacement velocity estimates.

A concise mathematical description of the strapdown decomposition, including the observation equations and uncertainty propagation is given in Sup. A.

[7]The median is inherently robust, meaning it is unaffected by point scatterers that deviate strongly from the RUM median velocity, beyond ±2 times the median absolute deviation (MAD).

2.3. Inter-track InSAR datum alignment

The strapdown method requires the contributing InSAR viewing geometries to be expressed in a common datum. In the absence of terrestrial control points for inter-track datum connection, we exploit a physical constraint characteristic of subsiding regions: *transversal velocities must be centripetal, i.e., directed toward increasing subsidence* (Kratzsch, 2012). A mismatch between track datums alters both the magnitude and sign of the decomposed (transversal, $\hat{d}_T$, and normal, $\hat{d}_N$) velocities, producing physically implausible results, such as transversal velocities pointing upslope and normal velocities indicating uplift, see Sup. C.

We use this constraint to jointly estimate the inter-track datum offset and the unbiased 3D velocities. The north component is therefore estimated within the physically constrained strapdown decomposition, rather than being resolved by the SAR viewing geometry alone. In practice, the inter-track datum alignment is performed by taking the descending track as reference.[8] A trial offset, $\Delta d^{\mathrm{asc}}_{\mathrm{LoS}}$, is applied to the ascending-track LoS velocities, the strapdown decomposition is recomputed for each trial, and the optimal offset is found by sampling the solution space of possible datum offsets and selecting the one that minimizes the number of negative transversal velocities

$$\min_{\Delta d^{\mathrm{asc}}_{\mathrm{LoS}}} \sum_{i=1}^{n} \mathbf{1}\Big(\hat{d}_{T_i}(d^{\mathrm{asc}}_{\mathrm{LoS},i} + \Delta d^{\mathrm{asc}}_{\mathrm{LoS}}, d^{\mathrm{dsc}}_{\mathrm{LoS},i}) < 0\Big), \tag{1}$$

where $i = 1, \ldots, n$ indexes the RUM observations, $d^{\mathrm{asc}}_{\mathrm{LoS},i}$ and $d^{\mathrm{dsc}}_{\mathrm{LoS},i}$ are the ascending- and descending-track LoS velocities for observation i, $\hat{d}_{T_i}(\cdot)$ is the resulting transversal velocity from the strapdown decomposition given the input LoS velocities, $\Delta d^{\mathrm{asc}}_{\mathrm{LoS}}$ is the trial offset applied to the ascending-track velocities, and $\mathbf{1}(\cdot)$ is an indicator function equal to 1 if the argument is true (i.e., if the transversal velocity is negative) and 0 otherwise.

The optimal offset, $\Delta \hat{d}^{\mathrm{asc}}_{\mathrm{LoS}}$, is determined by sampling the solution space of trial offsets within a pre-defined range, using increments of 0.1 mm yr^{-1} to match InSAR precision (2σ), and then identifying the global minimum analytically. The decomposition solution corresponding to this optimal offset produces physically consistent transversal and normal velocities, $\hat{d}_{T_i}$ and $\hat{d}_{N_i}$,

[8] The inter-track datum alignment procedure is independent of the choice of reference track; here, the descending track is used as the reference datum.

together with ENU velocity estimates and variance–covariance matrices in the local datum of the descending InSAR viewing direction.

2.4. InSAR and GNSS datum alignment

Since the decomposed ENU displacement velocities from the strapdown decomposition are expressed in the datum of the descending InSAR track, they must be converted to a terrestrial reference frame for geophysical interpretation. This is achieved using co-located RUMs, defined as RUM cells whose footprint contains at least one GNSS antenna. Within a co-located RUM, the point-like GNSS velocity in the chosen terrestrial reference frame—here the Sunda plate-fixed frame (Bock et al., 2003)—is assumed to represent the same deformation signal as the spatially averaged InSAR velocity obtained from the strapdown decomposition.

For each co-located RUM i, a 3D datum-connection vector is computed as the difference between the GNSS velocity in the Sunda Plate–Fixed Frame, $\hat{d}_i^{\mathrm{G|S}}$, and the RUM-averaged InSAR velocity in the local InSAR datum, $\hat{d}_i^{\mathrm{I}}$

$$\Delta d_i^{\mathrm{I}\rightarrow\mathrm{S}} = \hat{d}_i^{\mathrm{G|S}} - \hat{d}_i^{\mathrm{I}}, \tag{2}$$

where $\Delta d_i^{\mathrm{I}\rightarrow\mathrm{S}}$ is the 3D offset needed to align the InSAR-derived velocity of RUM i in the local InSAR datum (superscript I) with the corresponding GNSS velocity in the Sunda Plate–Fixed Frame (superscript G|S).

In the general case of multiple co-located RUMs, the final datum-connection vector, $\Delta d^{\mathrm{I}\rightarrow\mathrm{S}}$, and its uncertainty are estimated by a least-squares adjustment of all individual datum-connection vectors $\Delta d_i^{\mathrm{I}\rightarrow\mathrm{S}}$ derived from the RUM–GNSS pairs. The resulting best-fitting 3D offset is then applied uniformly to the entire InSAR velocity field, thereby connecting it to the chosen terrestrial reference frame. In the present study, the alignment is performed to the Sunda plate-fixed frame (S) using the only existing GNSS station in Jakarta spanning the study period (2014-2025), see Sec. 3. Consequently, the datum-connection vector is the 3D offset computed from a single co-located RUM, and added uniformly to all RUM velocities to express the InSAR-derived field in the Sunda plate-fixed frame

$$\hat{d}_i^{\mathrm{I|S}} = \hat{d}_i^{\mathrm{I}} + \Delta d^{\mathrm{I}\rightarrow\mathrm{S}}. \tag{3}$$

Here, $\hat{d}_i^{\mathrm{I}}$ is the RUM-averaged ENU velocity obtained from the strapdown decomposition and expressed in the descending InSAR datum, and $\hat{d}_i^{\mathrm{G|S}}$ is the ENU GNSS velocity in the Sunda plate-fixed frame. The uncertainties of $\Delta d^{\mathrm{I}\rightarrow\mathrm{S}}$ are derived through standard variance propagation, assuming independent uncertainties of the co-located GNSS and RUM-averaged InSAR velocities.

3. Results

3.1. Jakarta's 3D velocity field in the Sunda plate-fixed frame

To estimate three-dimensional land motion in Jakarta with associated uncertainties, the ascending-track datum is first aligned to the descending-track datum, establishing a common InSAR datum for both tracks. Following Sec. 2.3, a relative datum offset of $\Delta\hat{d}^{\mathrm{asc}}_{\mathrm{LoS}} = 1.2$ mm/yr is estimated by evaluating the objective function in Eq. (1) over all 4779 RUMs, with trial offsets sampled within the range $[-2.4,,2.4]$ mm/yr at 0.1 mm/yr increments. The optimal offset corresponds to the global minimum of this function, i.e., the minimum number of RUMs with negative transversal velocities[9]. The strapdown decomposition using this offset yields an intermediate 3D velocity field for Jakarta expressed in the common InSAR datum.

We connect this intermediate 3D velocity field to the Sunda plate-fixed frame following Sec. 2.4. The 3D datum connection vector is computed at the co-located RUM containing the CJKT GNSS station. Because CJKT is the only GNSS station covering the full 2014–2025 study period, this vector is obtained directly from the ENU velocity difference between the GNSS velocity in the Sunda plate-fixed frame and the decomposed co-located RUM velocity in the common InSAR datum, following Eq. (2).

The final datum connection is based on the assumption that the GNSS point velocity and the InSAR velocity of representative PS within the co-located RUM describe the same local deformation signal. In general, this assumption should be treated with caution because PS within the same RUM may correspond to ground-level objects, low-rise buildings, or taller structures whose motion can differ depending on foundation depth and structural coupling to the ground. Inspection of the original PS LoS velocities within the CJKT RUM, see Fig. 3, shows moderate velocity heterogeneity when all PS are considered (range $\sim$2.0 mm/yr, $\sigma = 0.5$ mm/yr, MAD = 0.4 mm/yr), and no strong correlation between PS velocities and their elevations. Using

[9]see Sup. animation rum_bias_animation_sup1.gif

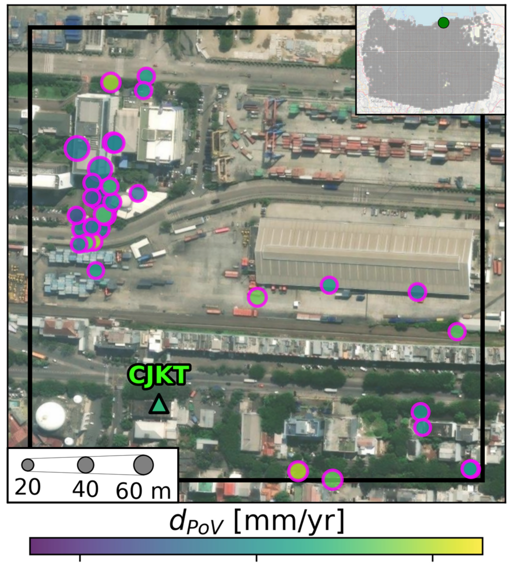

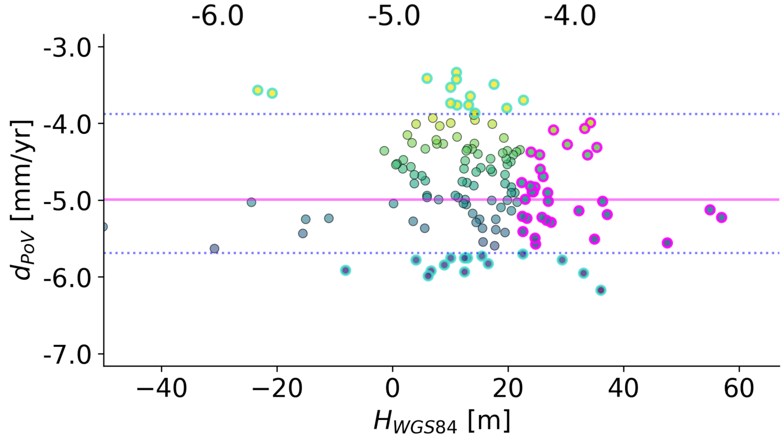

Figure 3: Height-based PS selection within the CJKT co-location RUM for establishing a precise datum connection to the Sunda plate-fixed frame. For visualization, LoS velocities from both tracks are first aligned to the common InSAR datum and projected onto the vertical direction. Although no strong correlation is observed between PS velocity and elevation, the known CJKT antenna height is used to select scatterers that are more structurally comparable to the GNSS monument. Selected PS satisfy $H_{\mathrm{WGS84}} \geq 22.205$ m, corresponding to the antenna height minus the 2σ Sentinel-1 PS height uncertainty. Relative to using all PS, this selection changes the estimated datum offset by ~ 0.3 mm/yr and reduces the empirical co-location uncertainty from approximately 2 to 1 mm/yr. **Top:** The 450×450 m co-location RUM, CJKT GNSS station, and selected PS are shown by the black outline, green triangle, and magenta-outlined points, respectively. Marker size scales with H_{WGS84}, and marker color shows d_{PoV}. **Bottom:** d_{PoV} versus H_{WGS84} for all PS. Magenta-outlined points are selected for datum connection, while light-blue outlined points are excluded. Dashed blue lines show the ± 2 MAD interval for all PS, and the magenta line shows the median LoS velocity of the selected PS.

all PS would therefore result in an empirical co-location uncertainty of approximately 2 mm/yr. Because the CJKT antenna is installed on a two-story concrete building and its antenna height is known, we use this information to preferentially select PS that are structurally comparable to the GNSS monument. Specifically, as the antenna is located at 32.205 m above the WGS84 ellipsoid, and Sentinel-1 PS heights have a formal 2σ-uncertainty of approximately 8–10 m (ESA/DLR, 2025), we select PS with $H_{\mathrm{WGS84}} \geq 22.205$ m to compute the RUM-averaged LoS velocity for each track prior to the decomposition. This selection is based on structural representativeness and reduces the empirical co-location uncertainty from $\sim$2 to 1 mm/yr.

The estimated 3D datum offset is applied component-wise to all RUM velocities in the ENU frame, transforming the strapdown-derived velocity field into the Sunda plate-fixed frame. The final 3D velocity map is shown in Fig. 4, with vertical velocities shown in color and directional horizontal, i.e., transversal, velocities shown as vectors. Only vectors with magnitudes greater than (2σ) are plotted, so that they represent statistically significant motion. The map clearly shows several subsidence bowls. Along the rims of the major bowls, outlined and numbered in turquoise in Fig. 4, horizontal velocities exceed 10 mm/yr and include distinct north components. These horizontal velocity vectors point toward the centers of the subsidence bowls (Kratzsch, 2012), indicating centripetal motion driven by sediment compaction. Such lateral motion may generate shear along bowl slopes and extension near bowl edges, potentially affecting building stability and increasing the vulnerability of underground pipelines.

3.2. Validation

As a full validation of the final 3D velocity field shown in Fig. 4 is not possible due to the lack of ground truth, we assess its agreement with co-located GNSS velocity estimates at station KBGN over 2023–2025, see Fig. 5. At KBGN, we compute the 3D ENU residual vector in the Sunda plate-fixed frame as

$$e_i = \hat{d}_i^{\mathrm{G|S}} - \hat{d}_i^{\mathrm{I|S}}, \tag{4}$$

where i denotes the co-located RUM. Uncertainties are propagated from the GNSS and InSAR ENU covariance matrices, assuming independent errors, and are reported as 2σ. The comparison shows millimeter-per-year agreement between GNSS and InSAR, with a vertical residual of 2.1 ± 2.9 mm/yr, a horizontal residual magnitude of 2.3 ± 1.9 mm/yr, and a 3D misfit of

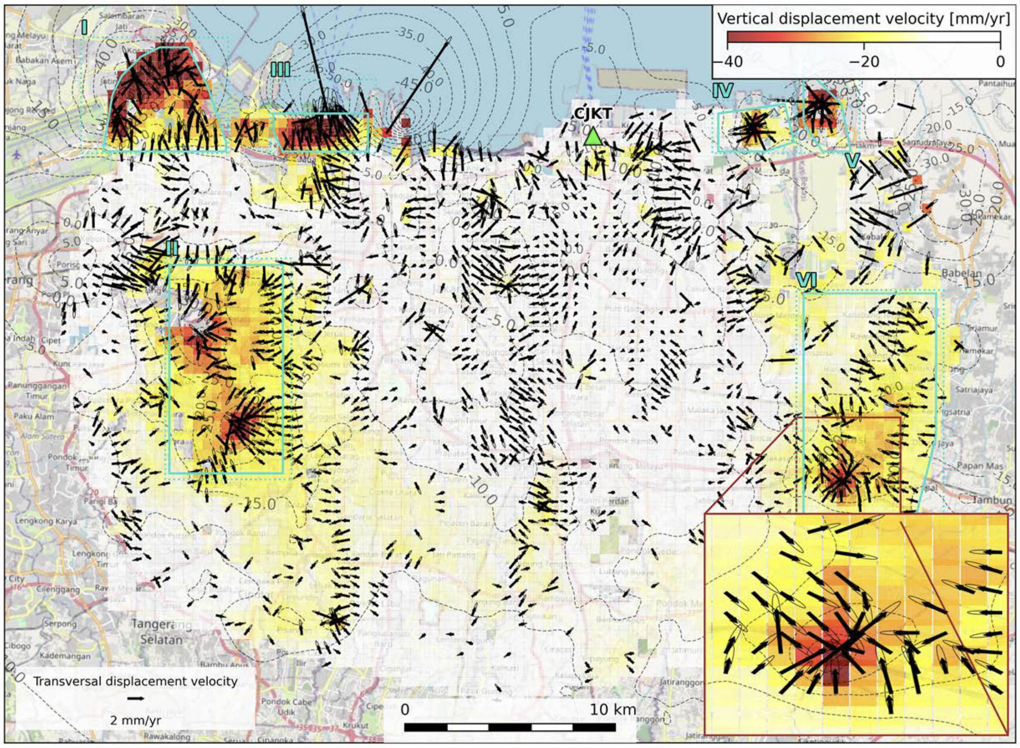

Figure 4: Sunda plate-fixed InSAR velocity map of the Jakarta metropolitan area (2014–2025) obtained via the single-station GNSS (green triangle) based datum connection. Vertical velocities are shown in color, and directional horizontal velocities are shown as vectors with 2σ confidence ellipses; only a subset of the vectors exceeding 2σ are displayed. Six major subsidence bowls (I–VI) are outlined in turquoise, while weaker subsidence patterns below $\sim$ 1 mm/yr (white) may also be present. Directional horizontal velocities near the bowl rims reach up to 10 mm/yr, including distinct north components. Central Jakarta shows little vertical subsidence compared to the bowls. The mean background subsidence rate outside the major bowls is -9.1 mm/yr. The inset in the bottom right corner zooms into Bowl VI, highlighting the centripetal horizontal velocity vectors; for a zoomed-in overview of each bowl see Sup. strapdown_zoomin_bowls.png. The corresponding decomposed 3D ENU velocity components and associated uncertainties are provided in Sup. ENU_field_plot.png.

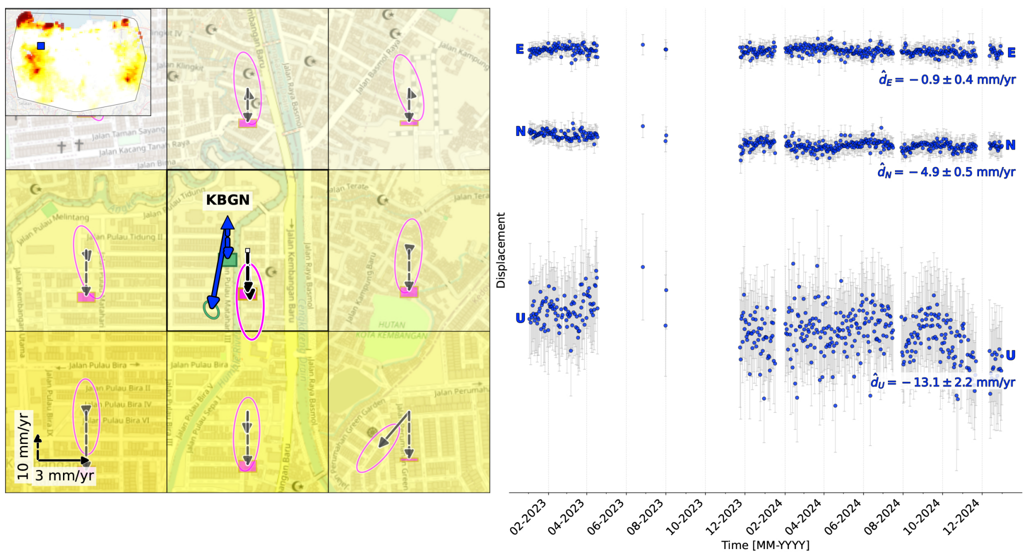

Figure 5: GNSS–InSAR validation of the final 3D velocity field in the Sunda plate-fixed frame at KBGN. The left panel shows the validation RUM containing the GNSS station and its neighboring RUMs, colored by RUM-averaged InSAR vertical velocity; the inset locates the validation RUM within the Jakarta-wide vertical velocity field. The blue arrow shows the GNSS velocity, and black arrows show the Sunda plate-fixed frame RUM-averaged InSAR velocities at each RUM centre; the central arrow is used for comparison. Filled and dashed arrows represent horizontal and vertical velocities, respectively, with green and magenta ellipses/intervals showing GNSS and InSAR (2σ) uncertainties. The right panel shows the 2023–2025 GNSS ENU displacement time series used to estimate the KBGN velocity. The comparison shows millimeter-per-year agreement between GNSS and InSAR, with a 3D misfit of 3.1 ± 2.4 mm/yr, providing site-specific validation of the final 3D velocity field at KBGN.

Table 2: Summary of mean and maximum vertical and directional horizontal (i.e., transversal) subsidence rates and cumulative displacements in Jakarta for each subsidence bowl, based on the CORS-based datum alignment. Velocities are in mm/yr, and cumulative displacements cover a 10.7-year period (October 2014 to June 2025) in mm.

Bowl #	**# RUMs**	$\hat{d}_{U_i}$ [mm/yr]			$\hat{d}_{T_i}$ [mm/yr]		
		mean	**max**	**max cum. [mm]**	**mean**	**max**	**max cum. [mm]**
I	112	−31.1	−55.9	−594.9	1.5	6.6	69.6
II	275	−21.9	−39.8	−423.4	1.0	3.8	40.4
III	44	−29.7	−78.5	−835.3	2.4	16.9	179.5
IV	32	−15.6	−35.1	−373.9	1.1	4.8	51.1
V	22	−26.0	−51.0	−542.6	2.1	9.8	104.0
VI	358	−17.1	−47.0	−500.2	0.7	5.8	61.7

3.1 ± 2.4 mm/yr. The horizontal velocity directions differ by $13.4° \pm 15.9°$, which is within the 2σ uncertainty. This millimeter-level 3D agreement is consistent with the linear subsidence behavior of the KBGN RUM over 2014–2025, which supports comparison of the final InSAR RUM-averaged velocity with the shorter 2023–2025 GNSS velocity, see Sup. B.

4. Discussion

4.1. Geophysical discussion

The 3D velocity map in the Sunda plate-fixed frame reveals six spatially localized subsidence bowls, labeled I to VI in Fig. 4 and outlined in turquoise. These bowls exhibit maximum vertical velocities of up to −78.5 mm/yr, and their subsidence characteristics are summarized in Tab. 2. Bowl III in the Muara Angke region shows the strongest deformation, with vertical velocities up to −78.5 mm/yr, a cumulative vertical displacement of −84 cm over the October 2014–June 2025 period, and transversal (i.e., directional horizontal) velocities up to 16.9 mm/yr that may pose risks to utility infrastructure. Bowl I, near Soekarno–Hatta International Airport, also exhibits severe vertical subsidence (maximum −55.9 mm/yr; cumulative −59 cm). The remaining four bowls show substantial but less extreme vertical motion. The six bowls span a variety of urban functions, including industrial areas, residential neighborhoods, commercial districts, and mixed-use zones. In the absence of a clear correlation, subsidence cannot be attributed to specific urban functions. The reported maximum vertical velocities and cumulative displacements are comparable with those of Harintaka et al. (2024), while about 28% lower than values reported by Sidiq et al. (2025). This difference reflect the methodological steps implemented here, namely the inter-track datum alignment, explicit connection to a terrestrial reference frame via GNSS, and the full 3D displacement decomposition that accounts for horizontal motion.

Several regions along the northern and northeastern coast of Jakarta, represented by the yellow RUMs in Fig. D.9B, exhibit higher intra-RUM velocity variability than the rest of the study area. This is evidenced by larger residual LoS velocities after removal of a planar trend within each RUM, as detailed in Sup. D. These areas correspond to densely built neighborhoods dominated by low-rise structures, likely supported by shallow or absent foundations, which experience slow subsidence with moderate spatial variability and lack the bowl-like velocity patterns characteristic of the major subsidence bowls, see Fig. 4. The observed velocity variability therefore points to a different subsidence mechanism, likely related to shallow subsurface processes. Two explanations are plausible: i) localized subsidence due to shallow groundwater extraction, or ii) slow consolidation of young coastal alluvium. Given that these regions are located in districts such as Tanjung Priok, Tambora, Pademangan, and Pluit—where municipal piped-water coverage is high and the phreatic aquifer is polluted (Taftazani et al., 2022)—shallow groundwater pumping is unlikely. Slow consolidation of young coastal alluvium is therefore the more probable mechanism.

Beyond the six subsidence bowls, the entire metropolitan area experiences slow regional subsidence, with a mean vertical velocity of −9.1 mm/yr across Jakarta.

The validity of the geophysical interpretation of Jakarta's subsidence depends on the quality of the final datum connection to the Sunda plate-fixed frame, anchored to the single CORS station at CJKT. As detailed in Sec. 3 and discussed further below, this connection is robust for the study period (2014–2025), with a co-location precision of ~ 1 mm/yr. However, relying on a single GNSS station in a dynamic urban environment has inherent limitations: changes in local building subsidence, or the relocation or destruction of the GNSS monument, could reduce the precision of future datum connections—or even prevent InSAR connection to the Sunda plate-fixed frame entirely. To support reliable long-term monitoring and rigorous InSAR–GNSS alignment, new infrastructure is urgently needed in Jakarta. Establishing multiple Integrated Geodetic Reference Stations (IGRS) (Hanssen, 2017), combining GNSS and corner reflectors visible in multiple InSAR geometries, would ensure precise ties and consistent alignment of the InSAR datum to the Sunda plate-fixed frame.

4.2. Geodetic discussion

Millimeter-scale misalignments between InSAR LoS datasets from different tracks can propagate through the strapdown decomposition and distort the estimated 3D velocity components. A sensitivity analysis for Jakarta, see Sup. C, shows that neglected inter-track datum offsets may produce biases in both magnitude and direction (including sign flips) of the transversal velocities, whereas normal velocities are affected only about one quarter as much in magnitude and roughly one tenth as much in direction. As the CJKT GNSS station exhibits millimeter-level residual horizontal motion after plate motion removal, see Fig. 2, using this station to align the ascending and descending LoS datums prior to the strapdown decomposition would propagate these residuals into the decomposed 3D velocities, particularly affecting the transversal velocities. To avoid introducing such errors from the earliest stage of the decomposition, the methodology in Sec. 2.3 instead exploits the high redundancy[10] of InSAR observations to simultaneously estimate 3D RUM-averaged velocities and perform inter-track datum alignment with sub-millimeter precision. This alignment is fully independent of GNSS data, providing a physically constrained and internally consistent means to tie multi-track InSAR observations to a common datum. GNSS observations at CJKT are used only for the final connection to the Sunda plate-fixed frame, as described later in this section.

The inter-track datum alignment assumes positive centripetal horizontal motion toward areas of increasing subsidence, a deformation-driven assumption in which gravity-driven compaction induces coupled vertical settlement and inward horizontal motion. For Jakarta, this is justified: the study area lies on coastal alluvial soils (Abidin et al., 2015; Colbran, 2009; Nugraha et al., 2024) with no known active faults crossing it, and the southward-dipping Baribis Fault (Gunawan et al., 2025), 50 km to the north, is too distant and oriented away to produce significant tectonic uplift or centrifugal horizontal motion. Consequently, the observed inward horizontal motion toward the centers of subsidence bowls is consistent with compaction-driven subsidence, likely linked to groundwater extraction (Kratzsch, 2012).

[10] > 50 PS per RUM per track across all 4779 RUMs

The strapdown decomposition in Jakarta relies on a spatially coherent deformation regime, where velocity change along iso-displacement lines is zero and radial velocity gradients within subsidence bowls define the local TLN orientation, enabling accurate 3D velocity reconstruction. To assess this coherence, a planar trend is fitted to the LoS velocities within each RUM, see Sup. D. Most RUMs (88%) show low residuals and semivariance after planar removal, with the strongest reduction inside the six major subsidence bowls, indicating that deep-seated, long-wavelength compaction dominates Jakarta's primary subsidence signal. By contrast, a small subset of RUMs, shown in yellow in Fig. D.9B, retains higher residual variability. In these RUMs, PS elevations vary by only ~ 20 m (2σ), and the LoS velocity variability remains within ± 3.5 mm/yr (2σ), indicating that the variability is not primarily elevation-dependent. These regions show slow subsidence, weak velocity gradients, and less well-resolved horizontal motion. This pattern suggests a different subsidence mechanism from that of the main bowls, most likely related to shallow subsurface processes such as consolidation of young coastal alluvium, as discussed earlier.

Beyond this spatial coherence in deformation, the use of period-average LoS velocities over 2014–2025 is consistent with the study objective of estimating full-period average 3D land motion. Nonlinear subsidence, see Sup. B, therefore does not invalidate the intended final 3D velocity field but only limits its interpretation over shorter time periods. For example, in accelerating areas, full-period average velocity estimates underestimate late-period rates and overestimate early-period rates, whereas the opposite holds in decelerating subsidence areas. Resolving such temporal changes would require an instantaneous or time-varying 3D decomposition, which is a relevant direction for future research. (Reviewer 1, Comment **??**)

In the final step, the strapdown-derived 3D velocity field is aligned to the Sunda plate-fixed frame using the CORS station at CJKT, the only long-term GNSS infrastructure available for datum connection in Jakarta, as confirmed by national geospatial authorities.[11] This step assumes that the GNSS point velocity and the InSAR velocity of selected PS within the co-located RUM capture the same deformation signal. To satisfy this assumption, the co-location RUM velocity is computed before decomposition using only PS at or above the CJKT antenna height. These roof-level or taller scatterers are

[11] Badan Informasi Geospasial (BIG) and Jakarta Survey Division

expected to behave similarly to the GNSS building, yielding a co-location uncertainty of $\sim$1 mm/yr for 2014–2025, see Fig. 3. This supports a reliable datum connection for the study period. However, future differential settlement or modifications to the structures hosting the selected PS or the GNSS monument could degrade or prevent this connection. Ensuring consistent, long-term alignment of InSAR-derived 3D velocity products to the Sunda plate-fixed frame will therefore require establishing multiple co-located GNSS–InSAR benchmarks across Jakarta.

5. Conclusion

Three-dimensional displacement velocities for Jakarta are estimated on a 450 $\times$ 450 m grid covering 2014–2025 and referenced to the Sunda plate-fixed frame, achieving millimeter precision that resolves detailed subsidence patterns beyond the capability of traditional GNSS or leveling surveys. All estimates are accompanied by a full variance–covariance matrix, allowing displacement significance to be assessed for groundwater management, flood-risk assessment, city planning and asset management.

Unlike previous InSAR studies relying on simplified geometric decompositions, this study produces, through a physically constrained strapdown decomposition, the first unbiased 3D velocity field for Jakarta. The velocity field shows that Jakarta's land motion is dominated by distinct subsidence bowls with extreme localized displacement, reaching a maximum vertical velocity of -78.5 mm/yr (Reviewer 1, Comment **??**). These bowls are superimposed on slower regional subsidence, characterized by a mean background vertical velocity of -9.1 mm/yr outside the bowl regions. Smaller coastal areas along the northern and northeastern shores show slower, spatially heterogeneous subsidence with no coherent bowl-shaped pattern. This suggests that shallow subsidence processes may be active in these areas, in addition to the deep-seated, long-wavelength compaction observed in the major bowls, with natural consolidation of young coastal alluvium as one possible mechanism. Localized directional horizontal displacements of up to 16.9 mm/yr are observed, providing statistically significant information for assessing deformation pathways and infrastructure risk.

The InSAR 3D velocity field is tied to the Sunda plate-fixed frame through the single long-term CORS GNSS station at CJKT, the only such infrastructure currently available in Jakarta. The selected high-elevation point scatterers co-located with CJKT provide a reliable datum connection for

2014–2025 with ~ 1 mm/yr precision. However, future settlement or structural changes at the selected point scatterers or the GNSS monument could affect long-term alignment. The deployment and maintenance of multiple co-located GNSS–InSAR benchmarks across Jakarta is therefore imperative for continued, accurate connection of InSAR-derived 3D velocities to the Sunda plate-fixed frame.

The findings demonstrate a novel procedure that combines strapdown decomposition of ascending and descending InSAR displacement velocities, a deformation-driven internal datum connection, and a GNSS-based InSAR datum alignment to a global terrestrial reference frame. This approach provides a comprehensive 3D subsidence monitoring method for Jakarta and establishes a transferable framework for other rapidly subsiding megacities, provided that spatially coherent deformation, suitable multi-track InSAR geometry, a physically justified internal datum constraint, and at least one reliable GNSS–InSAR co-location are available (Reviewer 1, Comment **??**). Effectively, careful InSAR datum alignment is as critical as the subsidence measurements themselves.

Supplementary material

Supplementary material is available for this article. In this review version, the appendices are included directly in the manuscript to provide reviewers with easy access to the supporting information; in the final version, these appendices are intended to form part of the supplementary material. In addition to the textual appendices, the supplementary material also includes a supplementary animation illustrating the iterative estimation of the inter-track datum offset, $\Delta\hat{d}^{\text{asc}}_{\text{LoS}}$, described in Sec. 2.3, as well as two additional figures containing input line-of-sight observations and zoomed bowl-scale visualizations. All supplementary items should be considered supporting information to the main article.

Acknowledgements

We thank Dr. F. van Leijen for valuable input on selecting InSAR processing parameters in DePSI. We also thank Bayu Triyogo Widyantoro, Sidik Tri Wibowo, and Febrylian Fahmi Chabibi from Badan Informasi Geospasial (BIG) for providing the GNSS data of the CORS station at CJKT in RINEX format.

Funding

This work was supported by the Dutch Research Council (NWO) through the Three SISTERS (grant no: NWO-WOTRO-482.21.505) project and by the Merian Fund Southeast Asia–Europe Joint Funding Scheme.

Declaration of Competing Interest

The authors declare that they have no known competing financial interests or personal relationships that could have appeared to influence the work reported in this paper.

Data availability

The final 3D ground displacement velocity estimates (east, north, up) for the Jakarta city and metropolitan area, including variance-covariance values are available at `https://doi.org/10.4121/39e7a39c-d305-425f-b238-1f3a4271dda9`. The North–East–Up GNSS time series of the CJKT CORS station are available from the Zenodo repository at `https://doi.org/10.5281/zenodo.7775016` (Susilo et al., 2023).

All other data and materials required to evaluate the conclusions of this study are included in the article and the supplementary material.

Author Contributions

A.M.L. contributed to Conceptualization, Methodology, Formal analysis, Investigation, Data Curation, Visualization, and Writing – Original Draft; designed the research, performed the analysis, created the figures, and wrote the first draft. H.A. contributed to Investigation, Resources, Data Curation, and Writing – Review & Editing; conducted, processed, and provided the GNSS data and additional metadata on the GNSS benchmarks. D.P. contributed to Investigation, Resources, and Data Curation; conducted, processed, and provided the GNSS data and additional metadata on the GNSS benchmarks. W.B. contributed to Methodology and Software; developed the strapdown method and provided feedback on its application. S.v.D. contributed to Investigation and Data Curation; processed the InSAR data. R.H. contributed to Supervision and Writing – Review & Editing; analyzed, reviewed, and edited the manuscript.

A. Mathematical Formulation of Strapdown Decomposition

The strapdown decomposition is used to estimate 3D displacement velocities from InSAR LoS velocity observations, following the approach of Brouwer and Hanssen (2024).

Let the vector of unknown parameters for each RUM be

$$x = [d_T, d_L, d_N, \Lambda, \Omega, \Phi]^T, \tag{A.1}$$

where d_T, d_L, d_N are the displacement velocities in the transversal, longitudinal (along the iso-displacement contour lines), and normal directions of the local TLN coordinate system, and Λ, Ω, Φ are the orientation angles of the TLN coordinate system, treated as pseudo-observation representing prior approximations for the TLN frame orientation.

The observations used to estimate these RUM-specific parameters are organized into $s = 1, \ldots, m$ sets, each corresponding to a distinct SAR viewing geometry (ascending or descending). These observations consist of RUM-averaged LoS velocities for each SAR viewing geometry and the pre-set TLN orientation angles, related to the unknowns through

$$E\{\begin{bmatrix} \underline{d}_{\text{LoS}}^{(1)} \\ \vdots \\ \underline{d}_{\text{LoS}}^{(m)} \\ \underline{\Lambda} \\ \underline{\Omega} \\ \underline{\Phi} \end{bmatrix}\} = \begin{bmatrix} a_1(x) \\ \vdots \\ a_m(x) \\ \Lambda \\ \Omega \\ \Phi \end{bmatrix}, \text{ with } a_s(x) = \left[P_T^{(s)}, P_L^{(s)}, P_N^{(s)}\right]_{\Lambda,\Omega,\Phi} \begin{bmatrix} d_T \\ d_L \\ d_N \end{bmatrix}, \tag{A.2}$$

where $P_T^{(s)}, P_L^{(s)}, P_N^{(s)}$ project the TLN velocities onto the LoS for all observations in set s.

For Jakarta, each RUM has two sets, corresponding to Sentinel-1 ascending track 98 and descending track 47. In the equations of the main text, the set index is indicated as a superscript: $s = \text{asc}$ for the ascending track and $s = \text{dsc}$ for the descending track. The RUM-averaged LoS velocity observations are computed as the robust median of all PS within each RUM (see Sec. 2.2) and, together with the pre-set TLN angles $\mathit{\Phi}$ and $\mathit{\Omega}$ (set to 0) and the longitudinal azimuth $\mathit{\Lambda}$ initialized from the 2D gradient of PoV velocities, are used to estimate the RUM-specific 3D displacement velocity parameters.

The dispersion of the observations is described by the covariance matrix

$$D\{\begin{bmatrix} \underline{d}_{\text{LoS}}^{(1)} \\ \vdots \\ \underline{d}_{\text{LoS}}^{(m)} \\ \underline{\Lambda} \\ \underline{\Omega} \\ \underline{\Phi} \end{bmatrix}\} = \begin{bmatrix} Q_{\text{LoS},1} & 0 & \cdots & 0 & 0 & 0 & 0 \\ 0 & Q_{\text{LoS},2} & \cdots & 0 & 0 & 0 & 0 \\ \vdots & \vdots & \ddots & \vdots & \vdots & \vdots & \vdots \\ 0 & 0 & \cdots & Q_{\text{LoS},m} & 0 & 0 & 0 \\ 0 & 0 & \cdots & 0 & \sigma_\Lambda^2 & 0 & 0 \\ 0 & 0 & \cdots & 0 & 0 & \sigma_\Omega^2 & 0 \\ 0 & 0 & \cdots & 0 & 0 & 0 & \sigma_\Phi^2 \end{bmatrix}, \tag{A.3}$$

where $Q_{\text{LoS},s}$ is the variance–covariance matrix of the RUM-averaged LoS observation in set s, derived via standard error propagation for the median averaging, and σ_Λ^2, σ_Ω^2, and σ_Φ^2 are the variances of the TLN pseudo-observation angles. For Jakarta, these are pre-set to $\sigma_\Lambda = 10°$ and $\sigma_\Omega = \sigma_\Phi = 3°$ (see Sec. 2.3).

The displacement velocity vector from x, $d_{\text{TLN}} = [d_T, d_L, d_N]^T$, is projected onto the LoS direction via a projection onto the plane orthogonal to the LoS, using the projector

$$P_{\text{LoS}^\perp}^R = [P_T, P_L, P_N], \tag{A.4}$$

with components

$$\begin{aligned} P_T = {} & (\sin\theta \sin\alpha_d \cos\Lambda - \sin\theta \cos\alpha_d \sin\Lambda)\cos\Omega \\ & - \Big((-\sin\theta\sin\alpha_d\sin\Lambda + \sin\theta\cos\alpha_d\cos\Lambda)\sin\Phi \\ & + \cos\theta\cos\Phi\Big)\sin\Omega, \end{aligned} \tag{A.5}$$

$$\begin{aligned} P_L = {} & (\sin\theta\sin\alpha_d\sin\Lambda + \sin\theta\cos\alpha_d\cos\Lambda)\cos\Phi \\ & + \cos\theta\sin\Phi, \end{aligned} \tag{A.6}$$

$$\begin{aligned} P_N = {} & (\sin\theta \sin\alpha_d \cos\Lambda - \sin\theta \cos\alpha_d \sin\Lambda)\sin\Omega \\ & + \Big((-\sin\theta\sin\alpha_d\sin\Lambda + \sin\theta\cos\alpha_d\cos\Lambda)\sin\Phi \\ & + \cos\theta\cos\Phi\Big)\cos\Omega. \end{aligned} \tag{A.7}$$

Here, θ denotes the incidence angle toward the radar, and α_d is the azimuth of the zero-Doppler plane at the target location, measured in the direction toward the satellite (Brouwer and Hanssen, 2023).

The unknown parameter vector x in Eq. (A.1) is estimated using an iterative Gauss–Newton approach applied to the observation model in Eq. (A.2).

At each iteration, the nonlinear equations are linearized around the current estimate and solved in a weighted least-squares sense until convergence is reached, yielding the final parameter estimates $\hat{x}$ and their associated covariance matrix $Q_{\hat{x}}$. The latter can be written in block-diagonal form as $Q_{\hat{x}} = \text{blockdiag}\big(Q_{\hat{\underline{d}}_{\text{TLN}}}, Q_{\hat{\underline{\Lambda}}}, Q_{\hat{\underline{\Omega}}}, Q_{\hat{\underline{\Phi}}}\big)$.

The estimated TLN displacement velocities $\hat{\underline{d}}_{\text{TLN}} = [\hat{\underline{d}}_T, \hat{\underline{d}}_L, \hat{\underline{d}}_N]^T$ and their covariance matrix $Q_{\hat{\underline{d}}_{\text{TLN}}}$ are subsequently rotated into the local East–North–Up (ENU) coordinate system using the estimated orientation angles $\hat{\underline{\Lambda}}$, $\hat{\underline{\Omega}}$, and $\hat{\underline{\Phi}}$

$$\mathbf{R}_{\text{TLN}\to\text{ENU}} = \mathbf{R}_{\hat{\underline{\Lambda}}}\,\mathbf{R}_{\hat{\underline{\Omega}}}\,\mathbf{R}_{\hat{\underline{\Phi}}}, \tag{A.8}$$

$$\mathbf{R}_{\hat{\underline{\Lambda}}} = \begin{bmatrix} \cos\hat{\underline{\Lambda}} & \sin\hat{\underline{\Lambda}} & 0 \\ -\sin\hat{\underline{\Lambda}} & \cos\hat{\underline{\Lambda}} & 0 \\ 0 & 0 & 1 \end{bmatrix}, \quad \mathbf{R}_{\hat{\underline{\Omega}}} = \begin{bmatrix} \cos\hat{\underline{\Omega}} & 0 & \sin\hat{\underline{\Omega}} \\ 0 & 1 & 0 \\ -\sin\hat{\underline{\Omega}} & 0 & \cos\hat{\underline{\Omega}} \end{bmatrix}, \quad \mathbf{R}_{\hat{\underline{\Phi}}} = \begin{bmatrix} 1 & 0 & 0 \\ 0 & \cos\hat{\underline{\Phi}} & \sin\hat{\underline{\Phi}} \\ 0 & -\sin\hat{\underline{\Phi}} & \cos\hat{\underline{\Phi}} \end{bmatrix}. \tag{A.9}$$

The ENU displacement velocities are obtained by rotating the estimated TLN velocities using $\mathbf{R}_{\text{TLN}\to\text{ENU}}$, i.e., $\hat{\underline{d}}_{\text{ENU}} = \mathbf{R}_{\text{TLN}\to\text{ENU}}\,\hat{\underline{d}}_{\text{TLN}}$, while the associated covariance matrix is propagated as $Q_{\hat{\underline{d}}_{\text{ENU}}} = \mathbf{R}_{\text{TLN}\to\text{ENU}}\,Q_{\hat{\underline{d}}_{\text{TLN}}}\,\mathbf{R}^{\top}_{\text{TLN}\to\text{ENU}}$, yielding the final 3D displacement components in the ENU coordinate system together with their full variance–covariance information.

For a full description of the equations and the estimation procedure, see Brouwer and Hanssen (2024).

B. Statistical hypothesis testing of linear LoS displacement behavior

We assessed whether an average linear velocity parameterization is representative of the 2014–2025 PS LoS displacement time series. The assessment was performed at the level of regions of uniform motion (RUMs), defined in Sec. 2.2 as 450×450 m spatial units within which deformation is assumed to be spatially constant. For each RUM, the PS LoS displacement time series were aggregated at each epoch by taking the median. This yields a RUM-averaged LoS displacement time series that describes the average displacement behavior of the RUM.

To assess linearity, a linear displacement model was fitted to the RUM-averaged LoS displacement time series for each RUM i and track $s \in \{\text{asc}, \text{dsc}\}$. The post-fit residuals were then tested against a prescribed track-specific LoS displacement uncertainty using an Overall Model Test (OMT) (Teunissen, 2024). The test statistic is

$$T_i^{(s)} = \frac{\sum_{t=1}^{n^{(s)}} \left(r_i^{(s)}(t) \right)^2}{\left(\sigma_{\text{LoS}}^{(s)} \right)^2}, \tag{B.1}$$

where $r_i^{(s)}(t)$ is the residual of the linear model at epoch $t = 1, \ldots, n^{(s)}$, $n^{(s)}$ is the number of valid epochs for track s, and $\sigma_{\text{LoS}}^{(s)}$ is the prescribed LoS displacement uncertainty for that track. The test was applied with a false-alarm probability of $\alpha = 0.05$, using $\sigma_{\text{LoS}}^{(s)} = 5.0$ mm for both ascending and descending tracks. The null hypothesis H_0 of linear displacement was rejected when

$$T_i^{(s)} > k_{\alpha=0.05, n^{(s)}-2}, \tag{B.2}$$

where $k_{\alpha=0.05, n^{(s)}-2}$ is the critical value for $n^{(s)} - 2$ degrees of freedom, corresponding to the fitted intercept and linear velocity. If H_0 was not rejected, the RUM was classified as linear for that track; otherwise, it was classified as nonlinear.

Across the combined ascending and descending OMT results, 92% of the evaluated RUMs are linear and 8% are nonlinear, see Tab. B.3. Nonlinear RUMs are mainly located within the outlined subsidence regions in Fig. B.6, which contain 58% of all nonlinear classifications. Among these regions, Region V has the highest nonlinear fraction, followed by Regions III and IV;

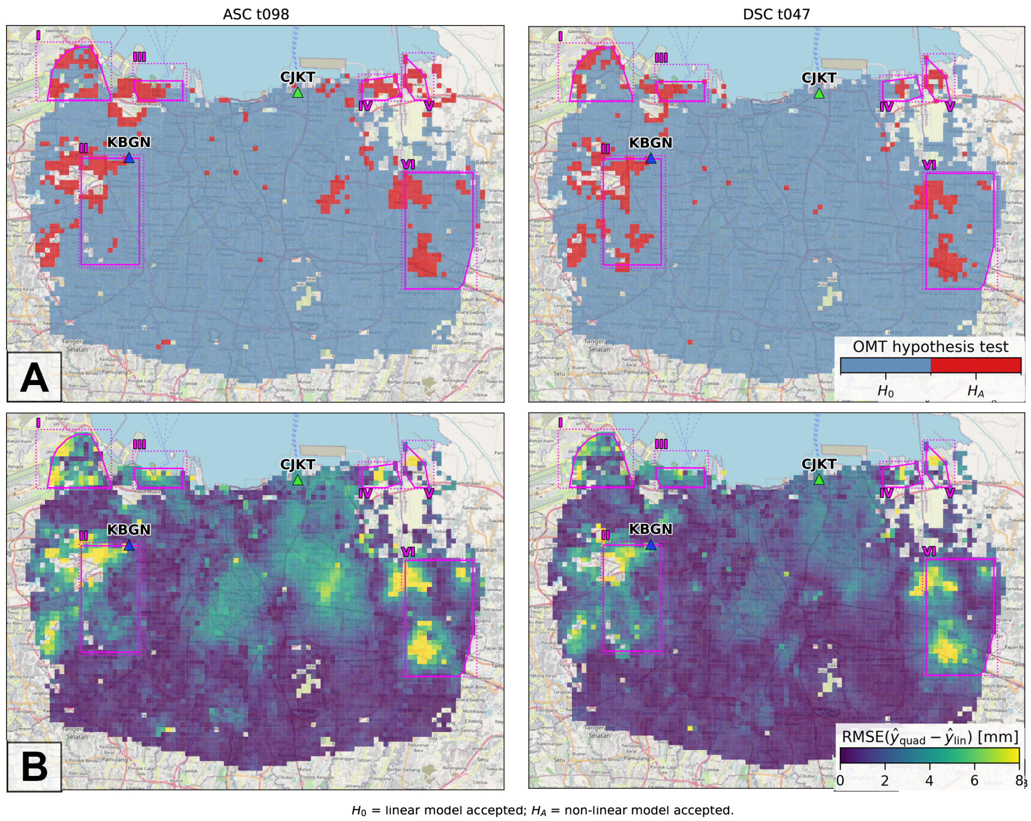

Figure B.6: Hypothesis testing of whether RUM-averaged LoS displacement time series can be represented by a linear displacement model over 2014–2025 for ascending track 98 and descending track 47. **A:** OMT classification for each RUM and track, using $\alpha = 0.05$ and a prescribed LoS displacement uncertainty of $\sigma_{\text{LoS}}^{(s)} = 5.0$ mm for both tracks; H_0 (light blue) denotes RUMs for which the linear displacement model is not rejected, whereas H_A (red) denotes nonlinear RUMs. **B:** Magnitude of deviation from linear behavior, computed as $\text{RMSE}(\hat{y}_{\text{quad}} - \hat{y}_{\text{lin}})$ between fitted quadratic and linear displacement models. Magenta outlines mark the main subsidence regions, corresponding to the turquoise outlines in Fig. 4. The CJKT datum-connection GNSS station is shown in green, and the KBGN validation GNSS station is shown in blue. Both CJKT and KBGN are located in RUMs showing linear subsidence behavior. Nonlinear behavior is mainly concentrated in and around the outlined subsidence regions.

Table B.3: Hypothesis testing classification of RUMs over 2014–2025 using the OMT. The OMT is applied separately to each RUM and track to test whether the linear displacement model is rejected. The table reports the combined ascending and descending results; therefore, one RUM can contribute up to two classifications. Percentages are computed relative to the number of classifications in each row.

Subset	**# classifications**	**Linear**	**Nonlinear**
Full RUM field	9558	8752 (92%)	806 (8%)
Inside subsidence regions	1686	1216 (72%)	470 (28%)
Region I	224	139 (62%)	85 (38%)
Region II	550	430 (78%)	120 (22%)
Region III	88	43 (49%)	45 (51%)
Region IV	64	35 (55%)	29 (45%)
Region V	44	10 (23%)	34 (77%)
Region VI	716	559 (78%)	157 (22%)
Outside subsidence regions	7872	7536 (96%)	336 (4%)

Regions I, II, and VI are predominantly linear. At the GNSS sites, both the CJKT datum-connection site and the KBGN validation site are located in RUMs showing linear subsidence behavior.

Overall, the predominance of linear RUMs supports the average linear velocity parameterization used to derive RUM-averaged LoS velocity observations for the strapdown decomposition. (Reviewer 1, Comment **??**)

C. Effect of inter-track datum misalignment on the relative velocity map of Jakarta

To quantify the impact of datum misalignment on the decomposed 3D velocity field, we compute both magnitude and directional (sign flip) residuals between the unaligned ($\Delta d^{\text{asc}}_{\text{LoS}} = 0$ mm/yr) and aligned ($\Delta \hat{d}^{\text{asc}}_{\text{LoS}} = 1.2$ mm/yr) decomposed velocity fields of each RUM, after the inter-track datum alignment, see Sec. 2.3. Magnitude residuals are defined as

$$\begin{aligned} \Delta\hat{d}_{T_i} &= \hat{d}_{T_i}\big(d^{\text{asc}}_{\text{LoS}_i}, d^{\text{dsc}}_{\text{LoS}_i}\big) - \hat{d}_{T_i}\big(d^{\text{asc}}_{\text{LoS}_i} + \Delta d^{\text{asc}}_{\text{LoS}_i}, d^{\text{dsc}}_{\text{LoS}_i}\big), \\ \Delta\hat{d}_{N_i} &= \hat{d}_{N_i}\big(d^{\text{asc}}_{\text{LoS}_i}, d^{\text{dsc}}_{\text{LoS}_i}\big) - \hat{d}_{N_i}\big(d^{\text{asc}}_{\text{LoS}_i} + \Delta d^{\text{asc}}_{\text{LoS}_i}, d^{\text{dsc}}_{\text{LoS}_i}\big). \end{aligned} \tag{C.1}$$

The magnitude bias is expressed as the Weighted Mean Absolute Bias (WMAB):

$$\begin{aligned} \text{WMAB}_T &= \frac{1}{n}\sum_{i=1}^{n} \big|\Delta\hat{d}_{T_i}\big|, \\ \text{WMAB}_N &= \frac{1}{n}\sum_{i=1}^{n} \big|\Delta\hat{d}_{N_i}\big|. \end{aligned} \tag{C.2}$$

Directional bias is quantified as the percentage of RUMs exhibiting a sign flip

$$\begin{aligned} \Delta\theta_T &= \frac{100}{n}\sum_{i=1}^{n} \mathbb{1}\Big(\hat{d}_{T_i}\big(d^{\text{asc}}_{\text{LoS}_i}, d^{\text{dsc}}_{\text{LoS}_i}\big)\cdot\hat{d}_{T_i}\big(d^{\text{asc}}_{\text{LoS}_i} + \Delta d^{\text{asc}}_{\text{LoS}_i}, d^{\text{dsc}}_{\text{LoS}_i}\big) < 0\Big), \\ \Delta\theta_N &= \frac{100}{n}\sum_{i=1}^{n} \mathbb{1}\Big(\hat{d}_{N_i}\big(d^{\text{asc}}_{\text{LoS}_i}, d^{\text{dsc}}_{\text{LoS}_i}\big)\cdot\hat{d}_{N_i}\big(d^{\text{asc}}_{\text{LoS}_i} + \Delta d^{\text{asc}}_{\text{LoS}_i}, d^{\text{dsc}}_{\text{LoS}_i}\big) < 0\Big), \end{aligned} \tag{C.3}$$

where $\mathbb{1}(\cdot)$ is the indicator function, which equals 1 if the argument is true (i.e., if the unaligned decomposed velocity has the opposite sign to the aligned decomposed velocity for the same RUM, their product will be negative) and 0 otherwise. For transversal velocities, the positive direction is defined as downslope (centripetal), while normal velocities are expected to be negative in sinking regions.

Fig. C.7 compares the unaligned and aligned decomposed velocities over the entire RUM field. Transversal velocities show a magnitude bias of $\text{WMAB}_T = 6.86$ mm/yr and directional flips $\Delta\theta_T = 33\%$, whereas normal velocities show smaller biases: $\text{WMAB}_N = 1.51$ mm/yr and $\Delta\theta_N = 2\%$.

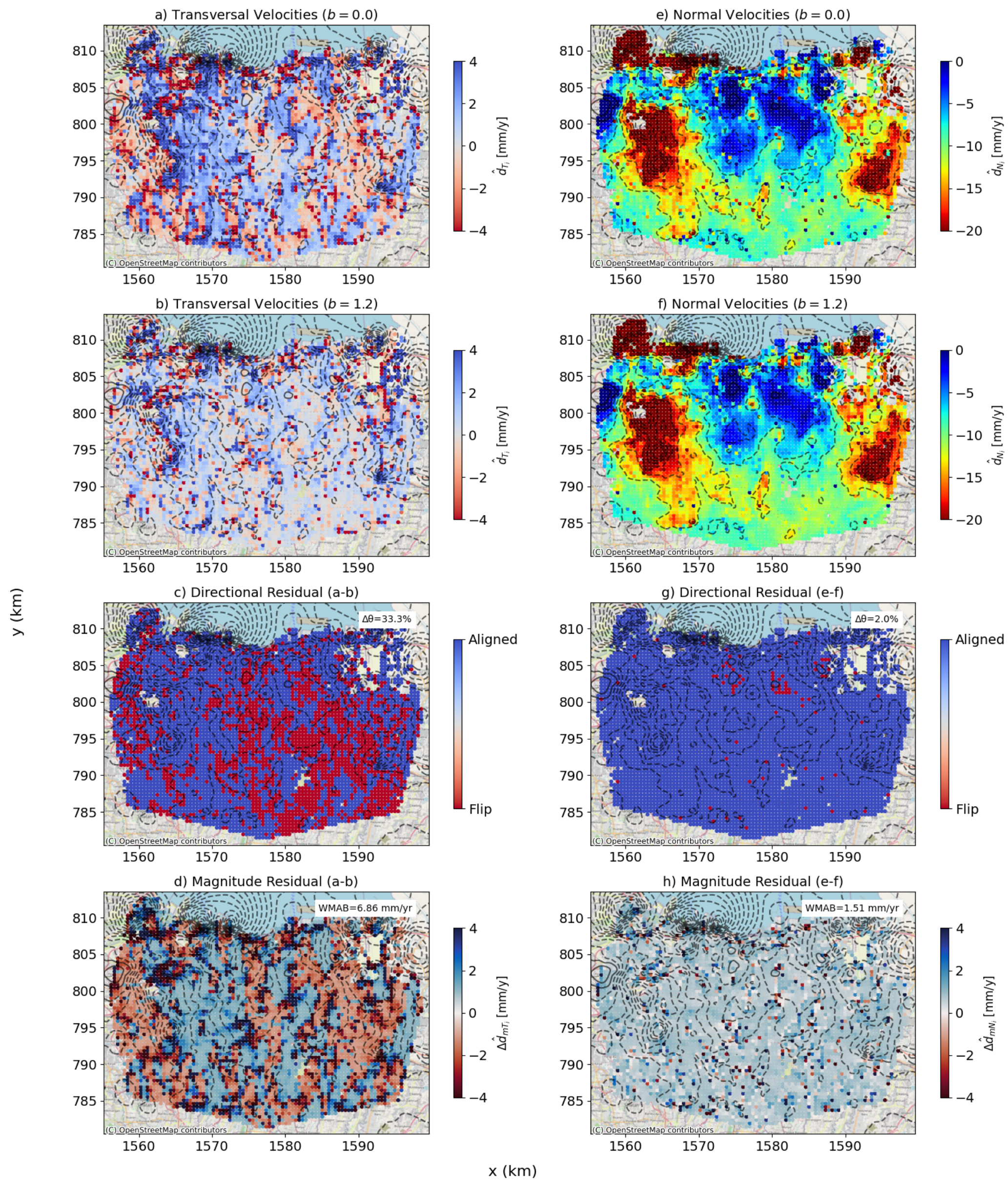

Figure C.7: Directional and magnitude biases due to inter-track datum misalignment in Jakarta. Columns show transversal (first) and normal (second) velocity components. Panels (a)–(b) compare unaligned ($\Delta d_{\mathrm{LoS}}^{\mathrm{asc}} = 0.0\,\mathrm{mm/yr}$) and aligned ($\Delta d_{\mathrm{LoS}}^{\mathrm{asc}} = 1.2\,\mathrm{mm/yr}$) transversal velocities; panels (e)–(f) show the same for normal velocities. Panels (c)–(d) and (g)–(h) display spatial variability of directional and magnitude biases.

Fig. C.8 shows the effect of varying the ascending track datum offset, $\Delta d_{\mathrm{LoS}}^{\mathrm{asc}}$, from -2.2 to $+2.2$ mm/yr in steps of 0.1 mm/yr. Transversal velocities reach up to 20 mm/yr (WMAB) and 45% directional flips, while normal velocities reach up to 4.8 mm/yr and 5% flips. Both magnitude and directional biases show a clear minimum at $\Delta d_{\mathrm{LoS}}^{\mathrm{asc}} = 1.2$ mm/yr, highlighting the necessity of proper datum alignment.

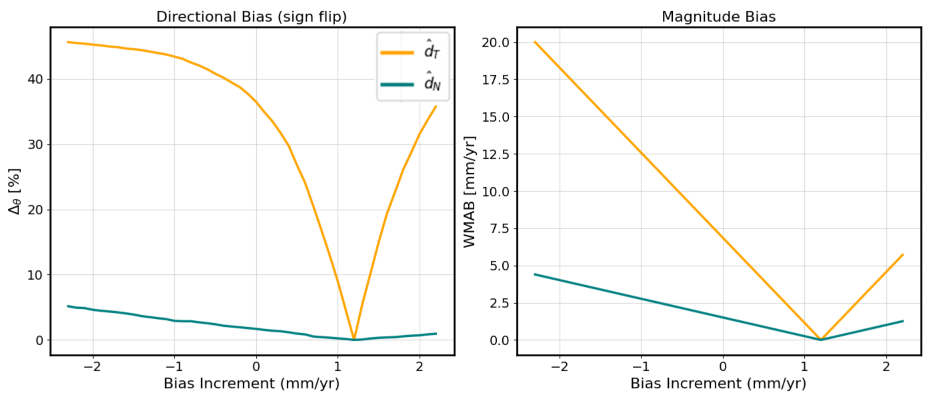

Figure C.8: Directional bias ($\Delta\theta$, left) and magnitude bias (WMAB, right) for transversal (T, orange) and normal (N, blue) velocity components across inter-track datum offsets. Transversal velocities are more sensitive, reaching 20 mm/yr (WMAB) and 45% ($\Delta\theta$). Both curves show a minimum at $\Delta d_{\mathrm{LoS}}^{\mathrm{asc}} = 1.2$ mm/yr.

D. Inter-RUM LoS velocity homogeneity assessment

Fig. D.9 evaluates intra-RUM LoS velocity homogeneity for the ascending and descending tracks to determine whether the estimated 3D velocity field of Jakarta (Fig. 4) reflects a spatially coherent subsidence regime. Within each RUM, homogeneity was assessed using the standard deviation of LoS velocities, the standard deviation and the semi-varianve $\gamma(h)$ of residual velocities after planar detrending. The semivariance lag was set to $h \approx 60$ m, determined by first computing the mean nearest-neighbor distance d_{nn} between PS points (~ 11 m ascending, ~ 9.5 m descending) and then incrementally evaluating the scale-dependent heterogeneity $H(n) = \gamma(n\, d_{\mathrm{nn}})/\sigma^2$ for increasing multiples n until the critical lag n_{crit} is reached. The critical lag n_{crit} is defined as the smallest n for which $H > 1$, indicating that local residual velocity variability exceeds the total RUM variance.

RUM velocities are considered spatially uniform—and therefore dominated by homogeneous, long-wavelength subsidence—if the LoS velocities are well described by a planar fit, with small residuals ($\sigma < 1$ mm/yr) and low semivariance ($\gamma < 0.8$ mm^2/yr^2). Approximately 88% of RUMs meet these criteria, especially within the six major subsidence bowls, highlighting areas dominated by deep-seated, long-wavelength compaction. In contrast, a small subset of RUMs along the northern and northeastern coasts (yellow regions in Fig. D.9B), including Tanjung Priok, Tambora, Pademangan, Pluit, and a north-south feature from Muara Baru to Central Jakarta, exhibits higher residual variability and semivariance. These areas are less spatially coherent and likely reflect different, shallower or more localized subsidence mechanisms, making the 3D velocity estimates there less well constrained.

References

Abdullah, F.M., Andriyanto, H., Nababan, J.R., Abdillah, F., Sulistyawan, R.I.H., 2021. Results of Land Subsidence Measurement using GPS Method in the Jakarta Groundwater Basin in 2015–2019, in: IOP Conference Series: Earth and Environmental Science, p. 012034. doi:https://doi.org/10.1088/1755-1315/873/1/012034.

Abidin, H., Djaja, R., Andreas, H., Gamal, M., Hirose, K., Maruyama, Y., 2004. Capabilities and Constraints of Geodetic Techniques for Monitoring Land Subsidence in the Urban Areas of Indonesia. Geomatics Research Australia 81, 45–58.

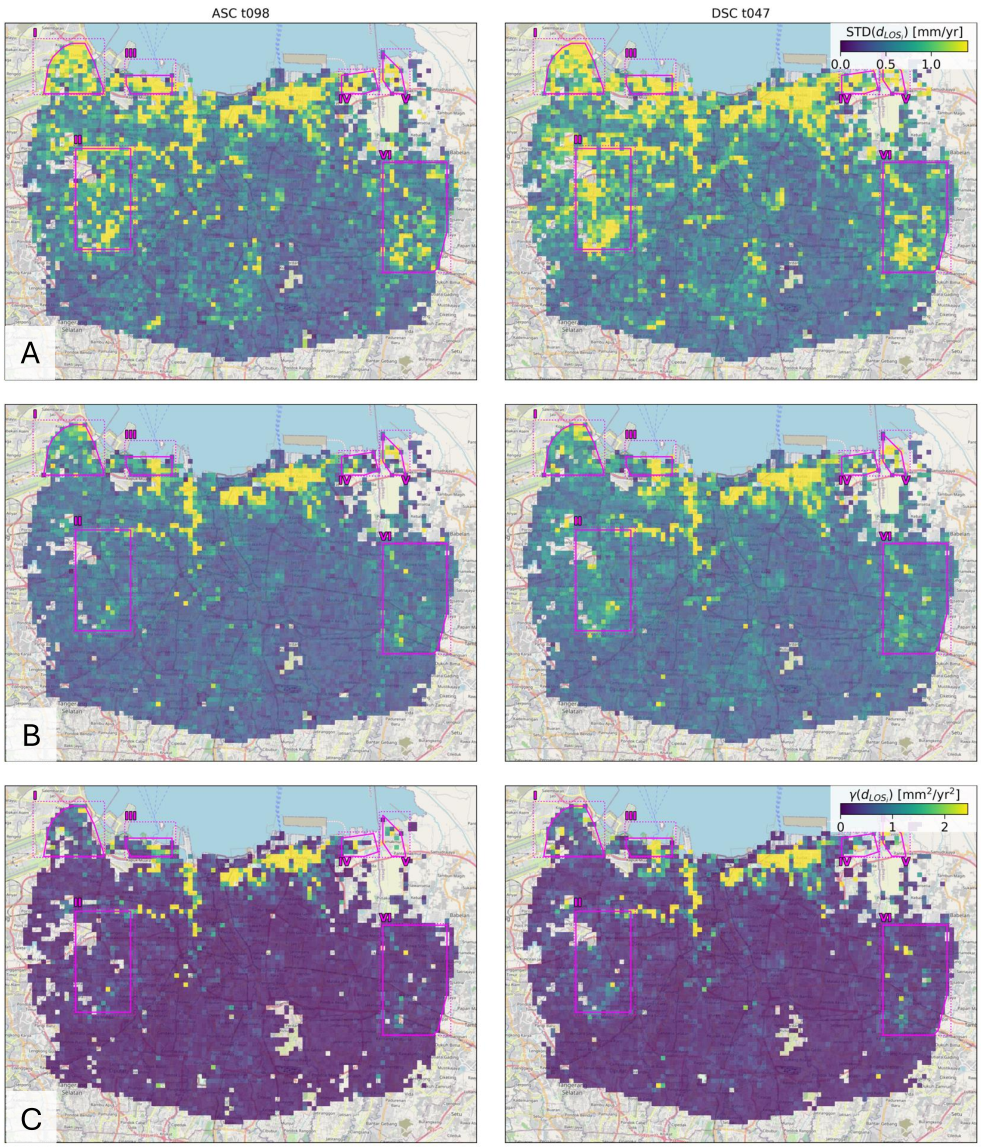

Figure D.9: Inter-RUM LoS velocity variability assessment. The six major subsidence bowls (outlined in turquoise in Fig. 4) are highlighted in magenta. **Row A:** Standard deviation of original ascending (left) and descending (right) LoS velocities at the RUM level. **Row B:** Standard deviation of residual velocities after removing a planar trend within each RUM. After plane removal, 88% of RUMs have $\sigma < 1$ mm/yr, with the largest reductions in the subsidence bowls, indicating long-wavelength, spatially coherent motion. **Row C:** Semivariance of residual velocities computed at a distance lag of $h \approx 60$ m, showing spatial correlation at short distances. Again, 88% of the AOI exhibits low semivarianc ($\gamma < 0.8$ mm^2/yr^2), while northeastern and northern coastal regions (yellow) retain higher residuals, suggesting subsidence there is not dominated by a uniform, deep-seated mechanism.

Abidin, H.Z., Andreas, H., Djaja, R., Darmawan, D., Gamal, M., 2008. Land Subsidence Characteristics of Jakarta between 1997 and 2005, as estimated using GPS Surveys. GPS Solutions 12, 23–32. doi:https://doi.org/10.1007/s10291-007-0061-0.

Abidin, H.Z., Andreas, H., Gamal, M., Djaja, R., Subarya, C., Hirose, K., Maruyama, Y., Murdohardono, D., Rajiyowiryono, H., 2005. Monitoring Land Subsidence of Jakarta (Indonesia) using Leveling, GPS Survey and InSAR Techniques, in: A Window on the Future of Geodesy: Proceedings of the International Association of Geodesy IAG General Assembly, Sapporo, Japan, June 30–July 11, 2003, pp. 561–566. doi:https://doi.org/10.1007/3-540-27432-4_95.

Abidin, H.Z., Andreas, H., Gumilar, I., Brinkman, J.J., 2015. Study on the Risk and Impacts of Land Subsidence in Jakarta. Proceedings of the International Association of Hydrological Sciences 372, 115–120. doi:https://doi.org/10.5194/piahs-372-115-2015.

Abidin, H.Z., Andreas, H., Gumilar, I., Fukuda, Y., Pohan, Y.E., Deguchi, T., 2011. Land Subsidence of Jakarta (Indonesia) and its Relation with Urban Development. Natural Hazards 59, 1753–1771. doi:https://doi.org/10.1007/s11069-011-9866-9.

Abidin, H.Z., Andreas, H., Gumilar, I., Sidiq, T.P., Pradipta, D., Yuwono, B.D., 2022. On the Disaster Risk Reduction of Land Subsidence in Indonesia's Northern Coastal Areas of Java, in: EGU General Assembly Conference Abstracts, pp. EGU22–1721. doi:https://doi.org/10.13140/RG.2.2.34300.00646.

Abidin, H.Z., Djaja, R., Darmawan, D., Hadi, S., Akbar, A., Rajiyowiryono, H., Sudibyo, Y., Meilano, I., Kasuma, M.A., Kahar, J., 2001. Land Subsidence of Jakarta (Indonesia) and its Geodetic Monitoring System. Natural Hazards 23, 365–387.

Batubara, B., Kooy, M., Zwarteveen, M., 2023. Politicising Land Subsidence in Jakarta: How Land Subsidence is the Outcome of uneven Sociospatial and Socionatural Processes of Capitalist Urbanization. Geoforum 139, 1–9.

Bennett, W.G., Karunarathna, H., Xuan, Y., Kusuma, M.S., Farid, M., Kuntoro, A.A., Rahayu, H.P., Kombaitan, B., Septiadi, D., Kesuma, T.N., et al., 2023. Modelling Compound Flooding: A Case Study from Jakarta, Indonesia. Natural Hazards 118, 277–305. doi:https://doi.org/10.1007/s11069-023-06001-1.

Berardino, P., Fornaro, G., Lanari, R., Sansosti, E., 2003. A new Algorithm for Surface Deformation Monitoring based on Small Baseline Differential SAR Interferograms. IEEE Transactions on Geoscience and Remote Sensing 40, 2375–2383. doi:https://doi.org/10.1109/TGRS.2002.803792.

Bock, Y., Prawirodirdjo, L., Genrich, J.F., Stevens, C.W., McCaffrey, R., Subarya, C., Puntodewo, S.S.O., Calais, E., 2003. Crustal Motion in Indonesia from Global Positioning System Measurements. Journal of Geophysical Research: Solid Earth 108. doi:https://doi.org/10.1029/2001JB000324.

Brouwer, W.S., Hanssen, R.F., 2021. An Analysis of InSAR Displacement Vector Decomposition Fallacies and the Strap-Down Solution, in: 2021 IEEE International Geoscience and Remote Sensing Symposium (IGARSS), pp. 2927–2930.

Brouwer, W.S., Hanssen, R.F., 2023. A Treatise on InSAR Geometry and 3-D Displacement Estimation. IEEE Transactions on Geoscience and Remote Sensing 61, 1–11. doi:https://doi.org/10.1109/TGRS.2023.3322595.

Brouwer, W.S., Hanssen, R.F., 2024. Estimating Three-Dimensional Displacements with InSAR: The Strapdown Approach. Journal of Geodesy 98, 110.

Chang, L., Dollevoet, R.P., Hanssen, R.F., 2018. Monitoring line-infrastructure with multisensor sar interferometry: products and performance assessment metrics. IEEE journal of selected topics in applied earth observations and remote sensing 11, 1593–1605.

Chaussard, E., Amelung, F., Abidin, H., Hong, S.H., 2013. Sinking Cities in Indonesia: ALOS PALSAR detects rapid Subsidence due to Groundwater and Gas Extraction. Remote Sensing of Environment 128, 150–161. doi:https://doi.org/10.1016/j.rse.2012.10.015.

Colbran, N., 2009. Will Jakarta be the next Atlantis? Excessive Groundwater Use resulting from a Failing Piped Water Network. Law, Environment and Development Journal 5, 18. URL: http://www.lead-journal.org/content/09018.pdf.

Ekkelenkamp, H., 2019. Indonesië op de Kaart: De Rol van de Nederlandse Aanwezigheid in Indonesië bij de Ontwikkeling van de Geodesie in Nederland .

ESA/DLR, 2025. Extension To Interferometry. Technical Note ETAD-DLR-TN-1006. European Space Agency (ESA) and German Aerospace Center (DLR). Issue 1.6.

Fenoglio-Marc, L., Schöne, T., Illigner, J., Becker, M., Manurung, P., Khafid, 2012. Sea Level Change and Vertical Motion from Satellite Altimetry, Tide Gauges and GPS in the Indonesian Region. Marine Geodesy 35, 137–150. doi:https://doi.org/10.1080/01490419.2012.674063.

Ferretti, A., Prati, C., Rocca, F., 2002a. Nonlinear Subsidence Rate Estimation using Permanent Scatterers in Differential SAR Interferometry. IEEE Transactions on Geoscience and Remote Sensing 38, 2202–2212. doi:https://doi.org/10.1109/36.868878.

Ferretti, A., Prati, C., Rocca, F., 2002b. Permanent Scatterers in SAR Interferometry. IEEE Transactions on Geoscience and Remote Sensing 39, 8–20. doi:https://doi.org/10.1109/36.898661.

Firman, T., Surbakti, I.M., Idroes, I.C., Simarmata, H.A., 2011. Potential Climate-Change related Vulnerabilities in Jakarta: Challenges and current Status. Habitat International 35, 372–378. doi:https://doi.org/10.1016/j.habitatint.2010.11.011.

Geng, J., Chen, X., Pan, Y., Mao, S., Li, C., Zhou, J., Zhang, K., 2019. PRIDE PPP-AR: An Open-Source Software For GPS PPP Ambiguity Resolution. GPS Solutions 23, 91. doi:10.1007/s10291-019-0888-1.

Gunawan, E., Widiyantoro, S., Hussain, E., Hanifa, N.R., Syafiudin, M.F., Wibowo, S.T., 2025. GNSS Constraints on the Jakarta Fault, Indonesia: Resolving Slip Rate and Seismic Hazard Potential. Earthquake Research Advances , 100424doi:https://doi.org/10.1016/j.eqrea.2025.100424.

Hakim, W.L., Achmad, A.R., Eom, J., Lee, C.W., 2020. Land Subsidence Measurement of Jakarta Coastal Area using Time Series Interferometry with Sentinel-1 SAR Data. Journal of Coastal Research 102, 75–81. doi:https://doi.org/10.2112/SI102-010.1.

Hanssen, R.F., 2001. Radar Interferometry: Data Interpretation and Error Analysis. Springer. doi:https://doi.org/10.1007/0-306-47633-9_4.

Hanssen, R.F., 2017. A radar retroreflector device and a method of preparing a radar retroreflector device. URL: https://patentimages.storage.googleapis.com/fe/ad/46/df362a63c8ed57/WO2018236215A1.pdf. patent WO 2018/236215 Al.

Harintaka, H., Suhadha, A.G., Syetiawan, A., Ardha, M., Rarasati, A., 2024. Current Land Subsidence in Jakarta: A multi-track SBAS InSAR Analysis during 2017–2022 using C-band SAR Data. Geocarto International 39, 2364726. doi:https://doi.org/10.1080/10106049.2024.2364726.

Herring, T.A., King, R.W., McClusky, S.C., et al., 2010. Introduction to GAMIT/GLOBK. Massachusetts Institute of Technology, Cambridge, Massachusetts 400, 401.

Hooper, A., 2008. A multi-temporal InSAR Method incorporating both Persistent Scatterer and Small Baseline Approaches. Geophysical Research Letters 35. doi:https://doi.org/10.1029/2008GL034654.

Hu, F., Wu, J., Chang, L., Hanssen, R.F., 2019. Incorporating temporary coherent scatterers in multi-temporal insar using adaptive temporal subsets. IEEE transactions on geoscience and remote sensing 57, 7658–7670.

Juliandri, F., Andreas, H., Pradipta, D., 2022. Efek Akurasi dan Geometrik Sistem Tinggi Digital Elevation Model (DEM) terhadap Pemodelan Banjir Rob di Jakarta. Bulletin of Geology 6, 934–948.

Kampes, B.M., 2006. Radar Interferometry: Persistent Scatterer Technique. Springer, Berlin.

Koudogbo, F.N., Duro, J., Arnaud, A., Bally, P., Abidin, H.Z., Andreas, H., 2012. Combined X- and L-Band PSI Analyses for Assessment of Land Subsidence in Jakarta, in: Remote Sensing for Agriculture, Ecosystems, and Hydrology XIV, pp. 46–58. doi:https://doi.org/10.1117/12.974821.

Kratzsch, H., 2012. Mining Subsidence Engineering. Springer Science & Business Media. doi:https://doi.org/10.1007/BF02509900.

Kreemer, C., Blewitt, G., Klein, E.C., 2014. A Geodetic Plate Motion and Global Strain Rate Model. Geochemistry, Geophysics, Geosystems 15, 3849–3889. doi:https://doi.org/10.1002/2014GC005407.

Lubis, S.W., Hagos, S., Hermawan, E., Respati, M.R., Ridho, A., Risyanto, Paski, J.A., Muhammad, F.R., Siswanto, Ratri, D.N., et al., 2022. Record-Breaking Precipitation in Indonesia's Capital of Jakarta in early January 2020 linked to the Northerly Surge, Equatorial Waves, and MJO. Geophysical Research Letters 49, e2022GL101513. doi:https://doi.org/10.1029/2022GL101513.

Mahapatra, P., van der Marel, H., van Leijen, F., Samiei-Esfahany, S., Klees, R., Hanssen, R., 2018. InSAR Datum Connection Using GNSS-Augmented Radar Transponders. Journal of Geodesy 92, 21–32. doi:https://doi.org/10.1007/s00190-017-1041-y.

Murdohardono, D., Sudarsono, U., 1998. Land Subsidence Monitoring System in Jakarta, in: Proceedings of Symposium on Japan-Indonesia IDNDR Project: Volcanology, Tectonics, Flood and Sediment Hazards, pp. 243–256.

Ng, A.H.M., Ge, L., Li, X., Abidin, H.Z., Andreas, H., Zhang, K., 2012. Mapping Land Subsidence in Jakarta, Indonesia using Persistent Scatterer Interferometry (PSI) Technique with ALOS PALSAR. International Journal of Applied Earth Observation and Geoinformation 18, 232–242. doi:https://doi.org/10.1016/j.jag.2012.01.018.

Nugraha, G.U., Bakti, H., Lubis, R.F., Nur, A.A., 2024. Jakarta Groundwater Modeling: A Review. Applied Water Science 14, 186.

Sagala, S., Lassa, J., Yasaditama, H., Hudalah, D., 2013. The Evolution of Risk and Vulnerability in Greater Jakarta: Contesting Government Policy. Institute for Resource Governance and Social Change, Kupang, Indonesia .

Schepers, J., 1926. De Nauwkeurigheidswaterpassing van Java, de Primaire Kringen 1a en ii, benevens het Stadsnet van Batavia en Weltevreden. Verhandelingen No. 1, Topografische Dienst in Nederlandsch-Indië .

Schuitenvoerder, H., 1926. De Nauwkeurigheidswaterpassing van Java. Jaarverslag van den Topografischen Dienst in Nederlandsch-Indië 1925.

Sidiq, T.P., Gumilar, I., Abidin, H.Z., Meilano, I., Purwarianti, A., Lestari, R., 2025. Spatial Distribution and Monitoring of Land Subsidence using Sentinel-1 SAR Data in Java, Indonesia. Applied Sciences 15. doi:https://doi.org/10.3390/app15073732.

Su, G., Xiong, C., Zhan, W., 2026. ID-GInSAR: An Improved Methodology for Integrating GNSS to Enhance InSAR-Based Deformation Monitoring. Geophysical Journal International 244, ggaf430. doi:https://doi.org/10.1093/gji/ggaf430.

Susilo, S., Salman, R., Hermawan, W., Widyaningrum, R., Wibowo, S.T., Lumban-Gaol, Y.A., Meilano, I., Yun, S.H., 2023. GNSS Land Subsidence Observations along the Northern Coastline of Java, Indonesia. Scientific Data 10, 421. doi:https://doi.org/10.1038/s41597-023-02274-0.

Taftazani, R., Kazama, S., Takizawa, S., 2022. Spatial Analysis of Groundwater Abstraction and Land Subsidence for Planning the Piped Water Supply in Jakarta, Indonesia. Water 14, 3197. doi:https://doi.org/10.3390/w14203197.

Takagi, H., Esteban, M., Mikami, T., Fujii, D., 2016. Projection of Coastal Floods in 2050 Jakarta. Urban Climate 17, 135–145. doi:https://doi.org/10.1016/j.uclim.2016.05.003.

Teunissen, P.J.G., 2024. Testing Theory: An Introduction. TU Delft Open.

United Nations, 2025. World Urbanization Prospects 2025: Summary of Results. Technical Report UN DESA/POP/2025/TR/NO. 12. United Nations, , Department of Economic and Social Affairs, Population Division. New York.

Van Leijen, F.J., 2014. Persistent Scatterer Interferometry Based on Geodetic Estimation Theory. Ph.D. thesis. Netherlands Geodetic Commission (NCG). Amersfoort, The Netherlands.

Widodo, J., Herlambang, A., Sulaiman, A., Razi, P., Perissin, D., Kuze, H., Sumantyo, J.T.S., 2019. Land Subsidence Rate Analysis of Jakarta

Metropolitan Region based on D-InSAR Processing of Sentinel Data C-band Frequency, in: Journal of Physics: Conference Series, p. 012004. doi:https://doi.org/10.1088/1742-6596/1185/1/012004.

Yong, C.Z., Denys, P.H., Pearson, C.F., 2017. Present-day kinematics of the Sundaland plate. Journal of Applied Geodesy 11, 169–178. doi:10.1515/jag-2016-0024.

Zebker, H.A., Villasenor, J., 1992. Decorrelation in Interferometric Radar Echoes. IEEE Transactions on Geoscience and Remote Sensing 30, 950–959. doi:https://doi.org/10.1109/36.175330.

Zhang, J., Duan, W., Fu, X., Yun, Y., Lv, X., 2025. The stepwise multi-temporal Interferometric Synthetic Aperture Radar with partially Coherent Scatterers for long-time Series Deformation Monitoring. Remote Sensing 17, 1374. doi:https://doi.org/10.3390/rs17081374.